

Modeling Surface Sensible Heat Flux Using Surface Radiative Temperatures in a Simple Urban Area

J. A. VOOGT

Department of Geography, University of Western Ontario, London, Ontario, Canada

C. S. B. GRIMMOND

Atmospheric Science Program, Department of Geography, Indiana University, Bloomington, Indiana

(Manuscript received 3 May 1999, in final form 7 December 1999)

ABSTRACT

Sensible heat fluxes over a light industrial area in Vancouver, British Columbia, Canada, are analyzed from observed tower fluxes and modeled using a bulk heat transfer approach. The bulk transfer models are initialized using remotely sensed surface temperatures from both airborne and ground-based observing platforms. The remotely sensed surface temperature, in conjunction with a surface database, is used to create area-weighted temperature estimates representative of the complete urban surface. Sensitivity analyses of the various surface temperature estimates are performed. Estimates of kB^{-1} , the ratio of roughness length of momentum to heat, for this area are in general agreement with theoretical estimates for bluff-rough surfaces and are larger than those documented for vegetated and agricultural surfaces. Back-calculated values do vary depending on the method used to determine surface temperature but vary more with the time of day. Empirical relations derived previously for vegetated surfaces are shown to agree well with the results for a dry urban environment. Approaches based on microscale variability in temperature fields are problematic.

1. Introduction

Much interest has been generated in the use of remotely sensed variables to estimate surface heat fluxes. Urban areas, both in terms of surface materials and morphology, provide a contrast to the wholly or partially vegetated systems that thus far have been the primary focus of study. In this study, observed surface sensible heat fluxes for a light industrial area within the city of Vancouver, British Columbia, Canada, are compared with modeled values based on bulk transfer or microscale variability approaches. The bulk transfer approach represents the surface as a single entity and employs bulk transfer equations applicable at the local scale (the bulk response) (e.g., Kustas et al. 1989). The microscale variability approach represents the surface as multiple entities, which then are aggregated within the local scale area (e.g., Sun and Mahrt 1995a).

The site chosen consists almost entirely of bluff-body elements with very little vegetation cover. The bluff-body elements differ less in their composition from the plane surface upon which they are built than is normally

the case for vegetation upon a soil surface. The general simplicity of the bluff elements (buildings) allows them to be represented as solid rectangular objects. Thus, the surface configuration can be simplified to a six-component system based upon geometric configuration and materials: roofs, four walls of given orientations, and ground-level surfaces. This approach makes the system more complex than the two-component system that may be applied to vegetation (e.g., Norman et al. 1995; Sun and Mahrt 1995a). The increase in surface components is offset by the ability to obtain detailed temperature observations representative of these surfaces, however.

The main objective of this study is to investigate bulk transfer and microscale temperature variability approaches for estimating sensible heat fluxes from an urban surface and compare the results with measured fluxes and results from other studies. In the implementation of both of these methods, we incorporate the flux source area model of Schmid (1994, 1997) to define appropriate source areas on the urban surface for extracting surface temperatures from the remotely sensed imagery. We also implement methods intended to provide more representative urban surface temperatures that explicitly include vertical surfaces within the flux source areas, and we assess the spatial variability of these temperatures and their effect upon modeled heat fluxes. We combine these procedures to produce estimates of the

Corresponding author address: Dr. James Voogt, Dept. of Geography, University of Western Ontario, London, ON N6A 5C2, Canada.
E-mail: javoogt@julian.uwo.ca

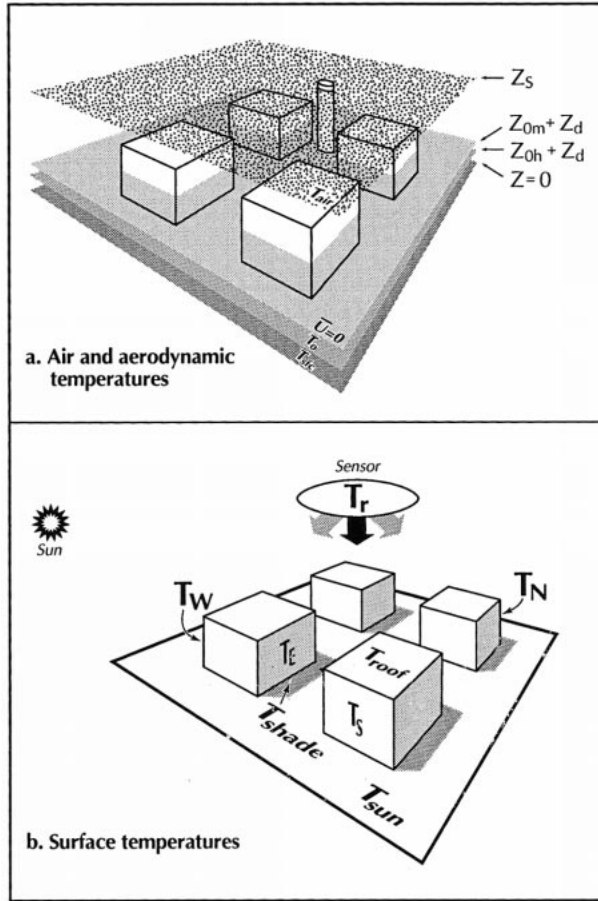


FIG. 1. Conceptual illustration of (a) surface definitions and levels and (b) component temperatures and remotely observed radiative temperature T_r , showing the effect of shading by buildings.

parameter kB^{-1} (defined below) over a simple, relatively unvegetated urban surface.

This paper reviews the modeling approaches in section 2 and describes the study site, observations, and methods of temperature representation in section 3. The results from the bulk surface modeling and microscale variability approach are contained in sections 4b and c, respectively. All variables used in this paper are described in the appendix.

2. Modeling approaches

a. The bulk surface response

The transfer of heat to, or from, the surface encounters more aerodynamic resistance than does momentum. To account for this, a bulk aerodynamic excess resistance r_b is defined (Verma 1989):

$$r_{ah} = r_{am} + r_b$$

$$= \frac{1}{ku_*} \left\{ \ln \left[\frac{(z_s - z_d)}{z_{0m}} \right] - \Psi_H \right\} + \frac{1}{ku_*} \ln \left(\frac{z_{0m}}{z_{0h}} \right), \quad (1)$$

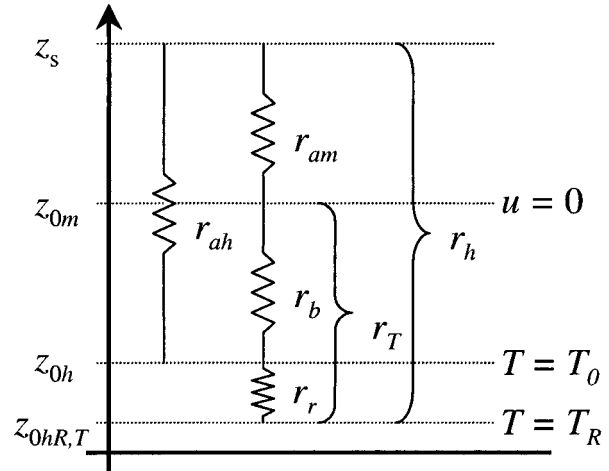


FIG. 2. Cross-sectional representation of the surface layer showing roughness lengths for momentum and heat and the resistances between different levels. The zero-plane displacement level z_d is omitted for simplicity. For some surfaces, $T = T_0 = T_R$ may be possible. Symbols are defined in the text.

where r_{am} is the aerodynamic resistance for momentum, r_{ah} is the aerodynamic resistance for heat, k is von Kármán's constant (0.4), u_* is the friction velocity, and Ψ_H is the stability correction for heat. The sensor height is z_s . The level at which the wind speed extrapolates to zero, via the logarithmic wind profile, is at $z_d + z_{0m}$ (the zero-plane displacement length plus the roughness length for momentum). Similarly, the aerodynamic surface temperature T_0 is the temperature extrapolated down to a surface that is at the height $z_d + z_{0h}$ (roughness length for heat). These surfaces are depicted graphically in Fig. 1. The local-scale surface sensible heat flux Q_H then can be calculated from the bulk transfer equation:

$$Q_H/C_a = (T_0 - T_a)/r_{ah} = (T_0 - T_a)C_H U, \quad (2)$$

where C_a is the volumetric heat capacity of air, T_a is the air temperature, C_H is the exchange coefficient for heat, and U is the wind speed. To implement (2), both T_0 and z_{0h} are needed, which are difficult to measure (Troufleur et al. 1997). However, it is possible to measure a radiometric surface temperature T_R and to replace T_0 in (2) (Stewart et al. 1994) so that

$$Q_H/C_a = (T_R - T_a)/r_h, \quad (3)$$

where, in addition, r_{ah} is replaced with r_h (Stewart et al. 1994):

$$r_h = r_{ah} + r_r, \quad (4)$$

and r_r is the radiometric excess resistance (Fig. 2).

The excess resistance from heat is expressed commonly in terms of kB^{-1} (Owen and Thomson 1963), where B^{-1} is a dimensionless parameter. The aerodynamic definition is

$$kB^{-1} = \ln \left(\frac{z_{0m}}{z_{0h}} \right), \quad r_b = \frac{B^{-1}}{u_*}. \quad (5)$$

Typically, a radiometric surface temperature is used rather than the aerodynamic surface temperature, and the resistance r_h is calculated as $r_h = r_{am} + r_T$ (Stewart et al. 1994), where $r_T = r_b + r_r$ represents the resistance between z_{om} and the surface (Fig. 2). Furthermore, the stability corrections for momentum and heat (Ψ_M and Ψ_H), which should be included in r_b [Verma 1989, Eq. (13)], rarely are incorporated. Thus, (5) is redefined as

$$kB^{-1}|_{R,T} = \ln\left(\frac{z_{om}}{z_{ohR,T}}\right), \quad r_T = \frac{B^{-1}|_{R,T}}{u_*}, \quad (6)$$

where the subscripts R and T make explicit the dependence of the results on the use of radiometric temperatures and the method for calculating the resistance [e.g., see also Trouffleau et al. (1997)].

A number of other methods are available to determine kB^{-1} , which rely to a greater or lesser extent on measured fluxes. These methods may be categorized broadly as (a) those that use Reynolds and sometimes also Prandtl numbers and (b) those that use additional information about the surface, for example, the anisothermal roughness length for heat [Brutsaert and Sugita 1996, Eq. (18), hereinafter referred to as BS96]. An example of the first approach is the Brutsaert [1982, Eq. (5.29)] equation for bluff-rough situations:

$$z_{oh,B82} = z_{om}[7.4 \exp(-2.46 \text{Re}_*^{0.25})], \quad (7)$$

where $\text{Re}_* = z_{om}u_*/\nu$ is the roughness Reynolds number, with a kinematic molecular viscosity ν of $1.461 \times 10^{-5} \text{ m s}^{-1}$.

Kubota and Sugita (1994) test the assumption that $z_{oh} = z_{ohR,T}$ for four periods of growth of a mixed pasture and conclude that “ $z_{oh} = z_{ohR,T}$ is not quite acceptable” for the entire stage of vegetation growth. They obtain the lowest correlations in the earliest and latest stages. In their approach, z_{oh} was determined from Brutsaert’s (1979) theoretical model. Although they provide a linear regression relation, it does not have general utility. BS96 have developed an equation based on Brutsaert’s (1979) model that expresses the roughness length for heat in terms of canopy structure, turbulence, and temperature. This approach takes into account the anisothermal heating, which is expressed as a function of the isothermal roughness length $z_{oh,I}$ with

$$z_{oh,I} = z_{om} \exp\left[\frac{z_h}{(z_h - z_d)r_2} + \ln\left(\frac{z_h - z_d}{z_{om}}\right)\right], \quad (8)$$

where z_h is the height of the roughness elements, and $r_2 = [a - (a^2 + 4C_2)^{0.5}]/2$. The anisothermal scalar roughness length is then expressed as

$$z_{oh,A} = z_{oh,I} \exp\left\{\frac{ku_*\rho c_p(T_g - T_h)}{Q_H} \left[\frac{(r_2 + b)C_2}{r_2(b^2 + ba - C_2)} + w\right]\right\}, \quad (9)$$

where ρ is air density, c_p is the specific heat capacity of air, T_g is the potential surface temperature near the

ground surface, T_h is the potential surface temperature near z_h (here taken to be the roof surface temperature), b is an extinction coefficient that ranges between 1 (isothermal) and 7 (steep temperature gradient) (BS96), and a is an extinction coefficient in the exponential shear stress profile that is about 1 for a sparse canopy and 3 for a dense canopy (BS96). Here the complete aspect ratio λ_c is used in coefficient C_2 :

$$C_2 = \frac{\lambda_c \text{Ct}_f z_h}{k(z_h - z_d)}, \quad (10)$$

where λ_c is the ratio of the complete surface area (the three-dimensional areas of vegetation and buildings) to the plan area, calculated using the method of Voogt and Oke (1997). The transfer coefficient Ct_f is given by

$$\text{Ct}_f = C_L \text{Re}_*^{-m} \text{Pr}^{-n}, \quad (11)$$

where C_L , m , and n are parameters that may depend on the shape and orientation of the roughness elements, and intensity of the turbulence which, following Verhoef et al. (1997), were set at 0.25, 0.25, and 0.36, respectively; and a Prandtl number Pr of 0.7 at 293 K (Verhoef et al. 1997) was used.

The w in (9) is a weighting parameter, which ensures that there is not undue variability in z_{oh} from the measurement strategy of the surface temperature. Practical measurement considerations usually dictate that T_0 as required by (2) is replaced by a remotely sensed radiative temperature T_R . If the surface is aerodynamically smooth and flat, T_0 may equal T_R . However, when the surface consists of an array of variously oriented surface elements, exposed to a wide array of irradiances and wind speeds, as in the urban environment, T_0 will not equal T_R (Huband and Monteith 1986; Trouffleau et al. 1997). In addition, significant measurement problems with T_R are incurred because of anisotropy of the emitted thermal radiation from rough surfaces when viewed by a narrow field-of-view instrument (Voogt and Oke 1997). According to BS96, the scalar roughness for an anisothermal surface (9) will remain the same as its isothermal value (8) when

$$T_R = wT_h + (1 - w)T_g \quad \text{and} \quad (12)$$

$$w = \frac{-(r_2 + b)C_2}{r_2(b^2 + ba - C_2)}. \quad (13)$$

To estimate a representative radiative temperature of the urban surface for the bulk surface representation, we first use the flux source area model of Schmid (1994, 1997) to define the area of the surface, which influences the tower-based measurement of Q_H . Then, within the source area, airborne and ground-based radiometric temperatures are combined in a geographic information system (GIS) framework to estimate a representative radiative source area temperature that combines temperatures of both horizontal and vertical surfaces. Further details are provided in section 3e. Following the spec-

ification of the surface temperature within the source area, we then can use the measured values of Q_H to back-calculate kB^{-1} .

An alternative approach that we test is that of Sun and Mahrt (1995b). They propose that, when radiometric temperatures are used in (2), C_H is replaced with C_{HR} . Variation in C_{HR} can be explained by

$$C_{HR} = a_{SM} \left(\frac{-T_*}{\Delta T} \right) = a_{SM} \left(\frac{-H/u_*}{T_R - T_a} \right), \quad (14)$$

where T_* is a temperature scale, and H is the kinematic heat flux. Based on the analysis of a number of tower- and aircraft-derived datasets of sensible heat flux and surface radiative temperature, Sun and Mahrt (1995b) found $a_{SM} = 0.11$, and $a_{SM} = 0.12$ when only the aircraft data are used. The differences are suggested to be due in part to different averaging methods. This result suggests that C_{HR} can be derived independently of the roughness length for heat. The single empirically determined curve suggested by (14) includes both the height dependence of the temperature difference ΔT and the effect of variable vegetation (surface) cover on ΔT . However, it is suggested that these dependencies do not strongly affect the coefficient a_{SM} . The roughness of the surface influences u_* but exerts only a secondary influence on C_{HR} , which can be expressed in terms of the drag coefficient C_D ,

$$C_{HR} = -C_D^{0.5} \frac{T_*}{\Delta T}, \quad (15)$$

which from (14) implies that $a_{SM} = C_D^{0.5}$. Similarly, Sun and Mahrt propose a relation for the radiometric roughness length for heat:

$$\ln(z_{ohr,T}) = c_1 + c_2(-\Delta T/T_*), \quad (16)$$

with coefficient values of 1.53 for c_1 and -0.37 for c_2 .

b. Microscale surface variations

The microscale variation approach takes into account the microscale distribution of surface radiation temperature (Sun and Mahrt 1995a, see also Malhi 1996). The bulk transfer coefficient C_{HR} can be calculated by assigning the roughness length for heat equal to that of momentum in (2). This equivalence avoids the simultaneous tuning of the relation for aerodynamic temperature and thermal roughness length (Sun and Mahrt 1995a). The surface (within the precalculated source area in this case) is divided into N different surface types, each with fractional area coverage f_i such that

$$\sum_{i=1}^N f_i = 1. \quad (17)$$

The aerodynamic temperature is related to the microscale surface distribution of surface radiation temperatures ($T_{R,i}$) by

$$T_0 = \sum_{i=1}^N \hat{g}_i f_i T_{R,i}, \quad (18)$$

where \hat{g}_i is the normalized heat conductance (the inverse of resistance) for the i th surface type, and g_i is the conductance for surface type i such that

$$\hat{g}_i = \frac{g_i}{g} = \frac{g_i}{C_H U}, \quad (19)$$

and the product $\hat{g}_i f_i$ in (18) is a weighting function subject to

$$\sum_{i=1}^N \hat{g}_i f_i = 1. \quad (20)$$

The aerodynamic temperature will, in general, be different from the spatially averaged surface temperature, which can be approximated as

$$\overline{T_R} = \sum_{i=1}^N f_i T_{R,i}. \quad (21)$$

In an urban area, the surface can be divided into a number of fractions, each with its own surface temperature (Fig. 1 and Fig. 12, described later): roof (f_r), north wall (f_n), east wall (f_e), south wall (f_s), west wall (f_w), sunlit street (f_{su}), and shaded street (f_{sh}). If vegetation is introduced, the fractions become more numerous. This approach can be simplified to consider the fraction that is sunlit (F_{sun}) or shaded (F_{sha}), subject to the constraint $F_{sun} + F_{sha} = 1$. The mean radiative temperature for the surface is

$$F_{sun} T_{sun} + F_{sha} T_{sha} = \overline{T_R}. \quad (22)$$

The relative fractions will change through the day because of varying sun-surface geometry. These fractions and the associated representative temperatures of the components are calculated within a given source area by using GIS and some simple rules about the presence or absence of shading.

3. Study description

a. Study area

The study area is a light industrial (LI) area (approximately 0.65 km²) within the city of Vancouver. The LI area is characterized by one-three-story buildings, most with flat roofs, and a notable lack of vegetation (plan area cover <5%). The buildings are arranged in city blocks, which have an east-west/north-south orientation, with the major block axis oriented east-west. Alleys run east-west between each street. Several blocks have buildings that share a common east-west wall, thereby reducing the exposed wall area. The average complete-to-plan area ratio (A_c/A_p ; also referred to as the complete aspect ratio λ_c) is 1.4. The complete area A_c is the total area of the urban surface, which

includes all horizontal and vertical surfaces, and A_p is the area of plan (horizontal) surfaces.

A database of building plan area was created by digitizing building outlines from aerial photographs and planning maps. The database includes 733 buildings. Building heights were estimated from the number of floors. The vector database was converted to a raster image with a $1 \text{ m} \times 1 \text{ m}$ resolution, and separate images of building roofs and walls (assumed to be of a north, south, east, or west orientation only) were created. For the analyses here, a reduced subset of the study area centered about the flux observation tower is considered. This area (which includes 517 buildings) extends 400 m west of the tower and 300 m to the north, south, and east, reflecting the predominant wind direction during the day, which varies from southwest to northwest. The average building height in this area is 6.9 m, with a standard deviation of 2.5 m. The distribution of building heights in the entire study area is presented in Voogt and Oke (1997).

b. Flux observations

Measurements were conducted in the framework of the surface energy balance. Instruments were mounted on a 28.5-m tower. Ancillary measurements of temperature, humidity, wind speed, and direction were made from a 9-m tower in close proximity. Net allwave radiation was measured using a Radiation and Energy Balance Systems, Inc., (REBS) Q*6 net pyr radiometer, and the turbulent sensible and latent heat fluxes were measured directly using the eddy correlation approach. The fast-response instruments, mounted less than 0.15 m apart, consisted of a Campbell Scientific, Inc., (CSI) one-dimensional sonic anemometer and fine-wire thermocouple system (CA27) to measure the fluctuations of vertical wind velocity and temperature and a CSI krypton hygrometer (KH20) to measure those of absolute humidity. The vertical wind velocity, air temperature, and humidity fluctuations were sampled at 5 Hz. Covariances were determined for 15-min periods. Flux corrections were made for oxygen absorption and air density (Webb et al. 1980; Tanner and Greene 1989; Tanner et al. 1993). No corrections were made for frequency response or spatial separation of the sensors. Fluxes and ambient meteorological conditions were measured for a period of 15 days, 11–25 August 1992, inclusive.

c. Flux source areas

A flux source area (or flux footprint) is the effective area on the ground that influences the measurement of a scalar flux. The model used here is the flux source area model (FSAM) described by Schmid (1994, 1997). This model calculates a source weight distribution function for a horizontal plane at the level of the zero-plane displacement height. This function defines the relative contribution of ground-level point sources to a flux mea-

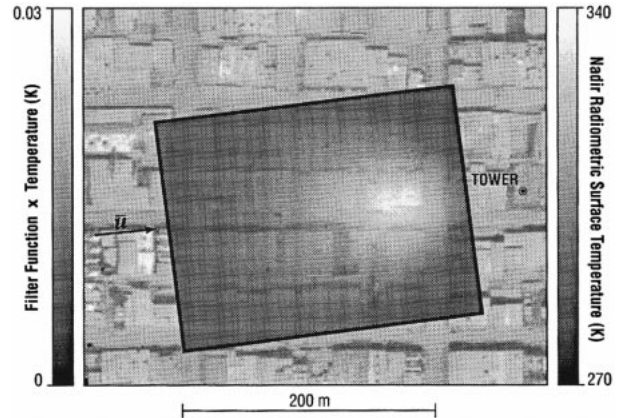


FIG. 3. Source weight function applied to composite nadir thermal image. LI area: 1300 LST 15 Aug 1992 (92/228).

surement made at a specified height and integrates to unity (Schmid and Lloyd 1999). The interpretation of this function is that a flux measured by a sensor can be represented as the weighted average of the point sources that make up the surface and that an appropriate averaging is defined by the convolution of the source area function with the surface source strength distribution (e.g., here temperature), by using the source area function as a linear, low-pass filter.

The source area model requires as input z_s , z_{om} , z_d , L (Obukhov length), and the acrosswind turbulence near the surface σ_v/u_* (Schmid 1994), where σ_v is standard deviation of crosswind velocity. Dimensions of the source area are dependent upon (in order of sensitivity): z_s/z_{om} (increases with height), stability [decreases as $(z_s - z_d)/L$ decreases], and σ_v/u_* (increases for increased crosswind turbulence) (Schmid and Lloyd 1999). The model assumes the surface to be flat and impermeable and does not take into account canopy geometry or within-canopy flows. Rough surfaces are handled simply through the general specification of the roughness length and zero-plane displacement (Schmid and Lloyd 1999). The radiative effects of vertical surfaces are included in the analysis by calculating an area-weighted urban surface temperature within the source area from off-nadir and vehicle-traverse temperature data (see section 3e).

FSAM source weight functions were calculated for the hourly observed conditions at the site for times that bracket the time of the remote-sensing overflight. This procedure yields two source areas for each of the three overflights for which surface temperature data are acquired. Typical input conditions for the majority of midday and late-afternoon times tested were $z_{om} = 0.26 \text{ m}$, $z_d = 3.1$, $\sigma_v/u_* = 2.0\text{--}3.0$ and $(z_s - z_d)/L = -0.68$ to -0.95 , which yield source areas ranging from 18×10^3 to $32 \times 10^3 \text{ m}^2$.

An example of a source weight function overlain on the composite thermal imagery is shown in Fig. 3, in which the source weight function values take on darker

tones for low values and are more transparent for higher values. These tones represent the three-dimensional shape of the source weight function, which exhibits an increasing value upwind of the sensor along the meanwind direction to a maximum and then decreases further upwind, with a symmetrical Gaussian shape in the crosswind direction.

d. Input variables

The variables used in calculations were derived in the following manner.

- 1) Roughness parameters were calculated using Raupach's (1992, 1994, 1995) method, as reported in Grimmond and Oke (1999a). The average values are $z_{0m} \approx 0.26$ m and $z_d \approx 3.1$ m.
- 2) Friction velocities, with stability corrections, were derived from tower measurements of U (log-law corrected to 30 m), T_a , and Q_H with an iterative solution as reported in Grimmond and Cleugh (1994).
- 3) Stability corrections for momentum and heat are the Paulson (1970) stability functions. For Ψ_M , when L is less than 0, the Högström (1988)-modified Dyer (1974) equation was used, and when L is greater than 0, the van Ulden and Holtslag (1985) equation was used. For Ψ_H , the Högström (1988)-modified Dyer (1974) equations were used.

e. Surface temperature

Radiative surface temperature data were collected using a combination of airborne and ground-based instrumentation to ensure adequate sampling of the major urban surface-component temperatures. A thermal scanner (AGEMA 880 long wave band), temporarily mounted in a helicopter, was used to obtain thermal images of the study area from both nadir and 45° off-nadir viewing angles in each of four viewing directions orthogonal to the main street orientation. Flights were made three times during 15 August 1992 (denoted as year/yearday 92/228) and four times in the period 1500 Pacific Daylight Time (PDT) 24 August 1992 (92/237)–0500 PDT 25 August 1992. Only daytime imagery is used in this study.

Imagery was corrected for atmospheric effects using locally launched radiosondes. Coincident ground-based sampling of select surfaces was performed as a check on the accuracy of the imagery. A summary of the flight details is provided in Table 1. Further details of the system configuration, flights, and correction procedures are provided in Voogt and Oke (1998a).

Corrections for surface emissivity were applied following image compositing (see below). In the absence of high-resolution data on surface type and radiative properties, a uniform surface emissivity of 0.95 was assumed (Arnfield 1982). The hemispheric incoming sky radiance in the scanner wave band was estimated

TABLE 1. Summary of helicopter flights over the study area (year is 1992).

Flight No.	Year/yearday and time (PDT)	Wind direction (°)	Altitude (m)	PDT plot time
1	92/228 1000	227	647–457	1000
2	92/228 1400	259	647–457	1400
3	92/228 1715	255	647–457	1700
9	92/237 1545	255	2100	1600

using the quadrature method of Lacis and Oinas (1991), with sky radiance modeled at 5 cm⁻¹ intervals using LOWTRAN-7 (low-resolution transmittance model and code, Kneizys et al. 1988) and the observed vertical profiles of temperature and humidity.

Building-wall temperatures in the study area were sampled using an array of infrared radiometers mounted on a vehicle (Voogt and Oke 1998b) that traversed all streets and alleyways in the study area. Corrections for surface emissivity were applied to the vehicle-traverse data using the methods outlined in Voogt and Oke (1998b). These take into account the effect of sensor position and the temperatures of the canyon facets. In addition, a set of fixed infrared sensors was used to monitor continuously the individual facets of select buildings near the flux observation tower.

Individual nadir images cover a limited area, so an image composite of the LI area was made. This procedure consists of identifying numerous (generally between 15 and 50) control points in both the nadir imagery and building footprint database, followed by resampling the imagery onto a common 1 m × 1 m template. A visual inspection of the remapped images was used to assess the suitability of the procedure. The final nadir image composite for flights 1–3 consists of 10–20 images. Off-nadir image composites were also made for each of the four view directions made. The image composite for flight 9 required only six images because of the much higher aircraft altitude.

SURFACE TEMPERATURE REPRESENTATIONS FOR URBAN AREAS

The composite thermal images provide high-resolution, spatially extensive surface temperature data. However, the images are limited in that each composite is associated with a particular view direction, which misses or undersamples portions of the “complete” urban surface (the full ground–atmosphere interface). Ideally, temperature information is required for all surfaces that make up the atmosphere–ground interface. Voogt and Oke (1997) generated estimates of the complete surface temperature T_c by combining frequency distributions of temperature obtained from airborne and ground-based observing systems, which were used to represent horizontal and vertical (wall) surfaces, respectively. Single estimates for the entire study area were calculated. To estimate T_c for a flux source area, a new method was

developed (Voogt 2000) using the remotely sensed data and a surface database (GIS). This method can be used to derive representations of surface temperature that take into account the three-dimensional structure of the buildings. Each of the representations combines nadir thermal imagery with temperatures of building walls derived from the vehicle traverses. Off-nadir imagery can also be used to estimate the building wall temperatures; these two methods show generally good agreement, with some differences observed because of the relative sensor position (Voogt and Oke 1997).

(i) *Area-weighted thermal images*

Area-weighted thermal images were constructed in which individual pixels represent the area-weighted temperature T_{aw} for both the horizontal and vertical surfaces associated with that pixel. The image was created by combining the building database, wall temperatures derived from vehicle traverses, and the composite nadir thermal imagery. Images of area-weighted temperature show cooler pixels that represent building edges, because those pixels represent not only the horizontal area of exposed roof but also the area of the wall below. Pixels that form corners of buildings are the most highly affected. Pixels that do not include a wall component are unaffected. Variations in the general method can be incorporated; for example, we have tested area-weighted temperature images that add only the projected windward wall areas of the buildings to the plan imagery.

(ii) *Complete surface temperature of source areas*

A complete surface temperature for a given spatial domain is the area-weighted temperature for an area that is sufficiently large to include the dominant surface structure (e.g., a building or block length). It therefore requires (a) the complete area within the domain and (b) temperatures of all surfaces within the domain. Here, the spatial domain used is that of the calculated flux source area.

The method implemented to calculate T_c is based upon prior calculation of an area-weighted thermal image. The area-weighted temperature image is multiplied by the image of total pixel area to recover the correct pixel-by-pixel temperature–area product. The sum of these pixels over the selected domain is divided by the total area of the domain to estimate T_c . An unweighted spatial average of the area-weighted temperature image is not equivalent to T_c . Notationally, we have

$$T_c = \sum_{j=1}^N \left[\sum_{i=1}^n A_i \left(\frac{\sum_{i=1}^n A_i T_i}{\sum_{i=1}^n A_i} \right) \right] / \sum_{j=1}^N \left(\sum_{i=1}^n A_i \right), \quad (23)$$

where A_i and T_i represent the area and temperature of surface elements i within a pixel containing n surface elements, and the outer summations are performed over the spatial domain defined by pixels $j = 1, N$, which

cover the flux source area. The numerator of the inner bracketed term in (23) represents the pixel area-weighted temperature image. The source weight distribution function can be incorporated in (23) by multiplying both the numerator and denominator of the inner bracketed term by the appropriate source weight for each pixel.

The final temperature representation used (T_{cb}) calculates a complete surface temperature for each building in the study area (rather than the flux source area itself) and applies the results to the plan area of each building. The remaining (plan) area temperature is specified by the nadir thermal composite image. This method provides an alternate temperature representation that may be convolved with the source weight distribution function to estimate a temperature within the source area.

4. Results

a. *Surface heat flux observations*

The synoptic conditions on both study days (92/228 and 92/237) were characterized by generally clear, sunny skies; warm temperatures; and a sea-breeze circulation—typical of the conditions for the full 15-day period during which energy balance measurements were made (Fig. 4). Lower-than-average air temperatures on day 237 can be explained by the passage of a cold front that day, which subsequently stalled and developed into a stationary front over central British Columbia. Air temperature on day 228 followed average conditions very closely until 0600. For the next 4 h (0600–1000), temperatures were warmer than average, reverting back to average values at 1100 with the onset of the sea breeze.

At this site, the sensible (Q_H) and storage heat fluxes (ΔQ_S) are the most significant output fluxes. As expected, the latent heat flux Q_E is very small. Daytime β values (Q_H/Q_E) were approximately 2.5. Grimmond and Oke (1999b) present a fuller discussion of the fluxes at this site relative to other urban areas.

In terms of conditions on the specific study days, the high sensible heat flux on day 228 at 0900 was the largest measured at that time during the study period. For much of the rest of day 228, however, Q_H was depressed relative to the ensemble. The surface temperatures (east and south walls especially) were warmer than average, as was the internal wall surface temperature (one facet was measured from an IR thermometer positioned inside the building). This result is consistent with the higher ΔQ_S flux observed that day. There were no synoptic disturbances that can explain the variability that was observed; the day was characterized by clear conditions of increasing pressure following the passage of a surface low and cold front two days earlier. This kind of hour-to-hour and day-to-day variability in fluxes is evident in energy balance data collected from a wide array of urban sites and is the subject of further investigation (see discussion in Grimmond and Oke 1999b).

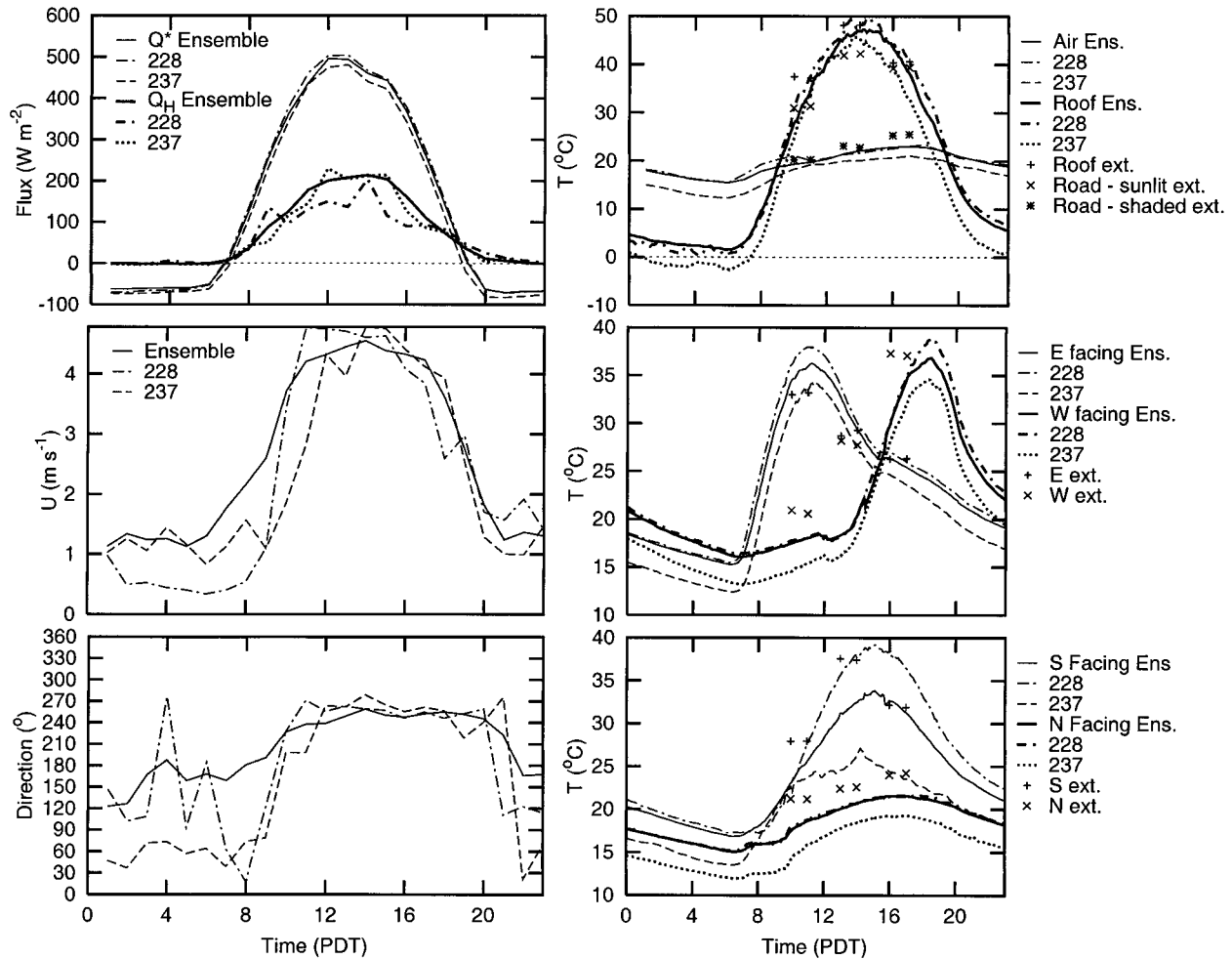


FIG. 4. Sensible heat flux (Q_H) and net allwave radiation (Q^*), wind speed (U), direction, air temperature (T_a), and E-W and N-S wall temperatures for 92/228, 92/237, and the ensemble mean (solid lines) for the full observation period. Extracted temperatures (ext.) are those from the remotely sensed data from overflights conducted on 92/228.

The sensible heat fluxes on day 237 (Fig. 4) were much more typical of the average conditions during the measurement period.

b. Results from the bulk approach

1) SURFACE TEMPERATURES FROM DIFFERENT METHODS

The bulk approach adopted in this paper is based upon a remotely measured surface temperature. In the analysis here, directional radiometric surface temperatures are modified to incorporate corrections for (a) atmospheric effects, (b) bulk surface emissivity effects, and (c) anisotropy (directional variations in observed emitted radiation caused by microscale patterns of temperature induced by the three-dimensional surface structure). Corrections for (a) and (b) are standard practice [e.g., see techniques and discussion by Byrnes and Schott (1986); Wan and Dozier (1989); Desjardins et al. (1990);

Prata (1994)]. The term “bulk” as applied to surface emissivity denotes the application of a single average emissivity rather than a pixel-by-pixel varying surface emissivity.

Because of the rough nature of the urban surface and the combination of viewing angles for a remote sensor, a large range of directional radiometric surface temperature measurements are possible (see section 3e). Figure 5 illustrates the range of temperature values calculated for the source areas using various definitions of the “surface” temperature. Two general categories of temperature estimates exist: 1) direct surface estimates from remote sensors (nadir and off-nadir temperature estimates), and 2) area-weighted temperatures (those which include information on the temperature of the building walls). Anisotropy is represented in Fig. 5 by the variability of directional radiometric temperatures (i.e., those that include atmospheric and emissivity corrections but do not take into account the surface struc-

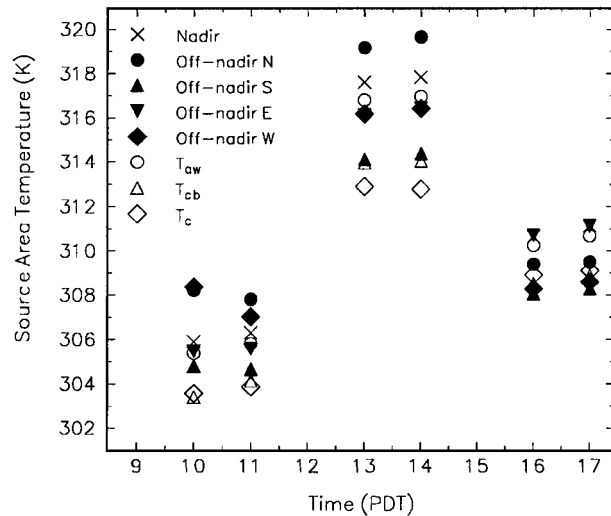


FIG. 5. Source area-weighted surface temperatures using various approaches to determine T_R for the three flights conducted on day 228.

ture) for the five view directions. All temperatures have been weighted by the source area weighting function applicable at the time for the tower-based measurements. These temperatures show a range of up to 5°C near midday (Fig. 5) at the scale of the flux source area. This range highlights the importance of surface structure and the effective anisotropy of surface thermal emissions.

Problems associated with anisotropy are addressed by estimating a radiometric temperature that includes the effects of vertical and horizontal surfaces (i.e., T_{aw} , T_c , or T_{cb}). The effect of including vertical surfaces into the source area temperatures yields a decrease in temperature; decreases are from 0.5° to 1°C when area-weighted temperatures are compared with nadir values, 2°–3.5°C when T_{cb} is used, and 2°–5°C when T_c is used.

Spatial variability

In this section, the spatial variability of the bulk surface temperature representation (temperature calculated for the domain of a flux source area) is assessed. Flux source area position depends upon the wind direction, and the source area size is a function of measurement height, thermal stability, and crosswind turbulence intensity and the surface structure (Schmid 1994).

To evaluate the effect of source area position upon the source area-averaged temperature, two tests were performed. In the first, a flux source distribution function (and flux source area) is calculated for a given set of conditions (here we use those for 1400 PDT, 92/228). This source area is rotated about the tower to simulate the source area position for different wind directions (but similar measurement height, stability, crosswind turbulence, and general surface structure). The source weight distribution function then is convolved with the image of T_{aw} , and the resultant source area temperature

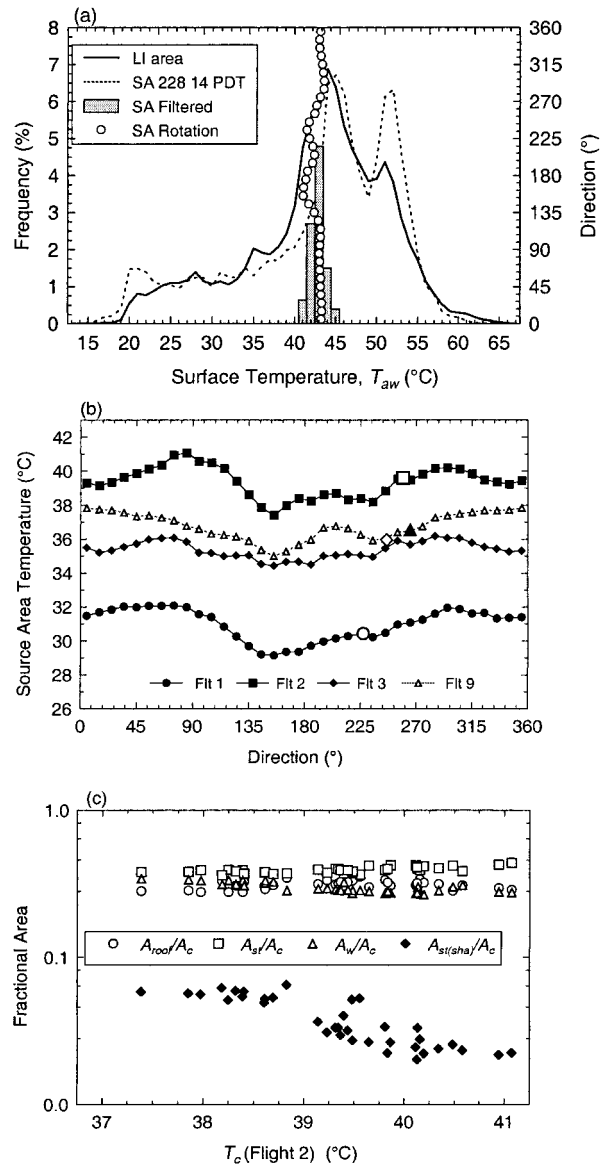


FIG. 6. (a) Surface temperature variability as determined by T_{aw} for flight 2 at 1400 (92/228). Solid line is the frequency distribution of surface temperatures for the entire image, dashed lines are the frequency distribution for the source area, histogram is the frequency distribution of surface temperatures when the entire image is filtered by the source weight distribution function, and open circles are the average surface temperature for the source area rotated around the tower. (b) Source area temperature from rotation of the source area about the tower for flights 1–3 (T_c) and flight 9 (T_{nadir}). (c) Fractional component areas within rotated source area plotted vs T_c . Symbols are A_c : complete area, A_{roof} : roof area, A_w : wall area, $A_{st(sha)}$: shaded street (ground level) area.

is recorded. These results are shown as empty circles in Fig. 6a. The frequency distribution of T_{aw} (from individual pixel values) for the entire study area (solid line) as well as within the calculated flux source area (dashed line) is also plotted for comparison. A similar test is performed by using source areas calculated for

each flight on 92/228 and by calculating T_c for each source area position (Fig. 6b). Results for flight 9 are also shown in Fig. 6b; these results display the average nadir temperature from the source area, because wall surface temperatures were available for only a single building on that day.

The second test uses the calculated source weight distribution function as a filter. This filter is applied to the entire image, and the resultant image is analyzed. This process is analogous to a low-pass filtering operation, except the weights for the filter array in this case are not equal but rather are specified from the source weight distribution function (see also Schmid and Lloyd 1999). Temperatures from the resultant image are extracted (edge effects are masked) and are plotted as the frequency distribution represented by shaded bars in Fig. 6a. To speed the filtering operation and to accommodate the filter size, the image and filter resolution is degraded to $5 \text{ m} \times 5 \text{ m}$.

The results of these two tests show spatial variability of up to 5°C near midday based upon source area position. This variability is reduced later in the day when the overall range of surface temperatures narrows and the source area increases in size. The rotation test shows a consistent pattern related to the temperature structure of the ground. Temperature minima are observed when the source area fraction of shaded area increases from either the height and/or spacing of the buildings (Fig. 6c). Local maxima in temperature are observed for directions in which there are shorter buildings with large plan-to-complete area ratios and/or for which street areas dominate. Some of the source area temperature variability could be traced to individual buildings with extreme temperature values such as a very hot roof or a roof with a low surface emissivity, not accounted for in the correction procedure. These tests demonstrate that using the source area concept is an important step in specifying the most appropriate surface temperature for use in the bulk heat transfer equation.

Source area size is coupled to atmospheric and surface conditions. Thus, direct observation of the variability of source area temperature for changing source area dimensions is not strictly possible without thermal imagery taken under each of the conditions to be tested. In the absence of this coupled information, a test of the variability of T_c within various domain sizes, which have as their starting point different components of the urban surface, was performed. For simplicity, square domains ranging from $3 \text{ m} \times 3 \text{ m}$ to $251 \text{ m} \times 251 \text{ m}$ were used with equal weightings applied to all points. The domain midpoints were selected to be middle of a street intersection, middle of a roof, midpoint of an east–west alleyway, and the flux observation tower. In accordance with previous results (Schmid and Oke 1992), the majority of variability is at small scales, in this case well within the source area size dimension (Fig. 7). Notably, most of the temperature variation is confined to length scales less than 60 m. Variability in T_c at different spatial

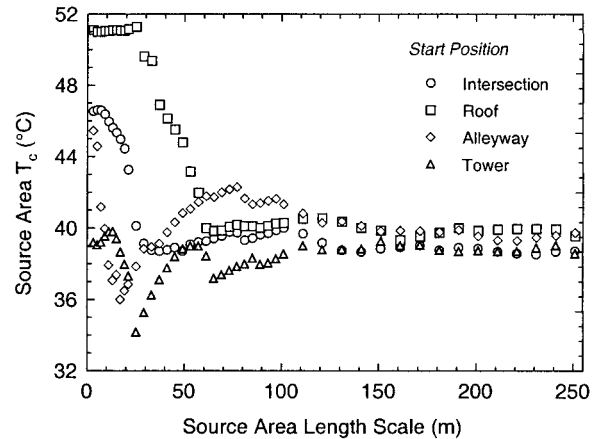


FIG. 7. Mean unweighted complete source area temperature (T_c) for increasing square domain source area sizes for four starting points (midroof, midstreet, midalleyway, and the tower).

scales for this study area is similar to that of directional temperature measurements (e.g., T_{nadir}). This similarity results from the fact that the dominant control on the variability is the surface structure, and the breakpoints at which major temperature changes occur (building, lot, and block scales) remain the same. The effect of including building wall temperatures does not alter the range of observed surface temperatures, nor does it add a new spatial scale of temperature variability.

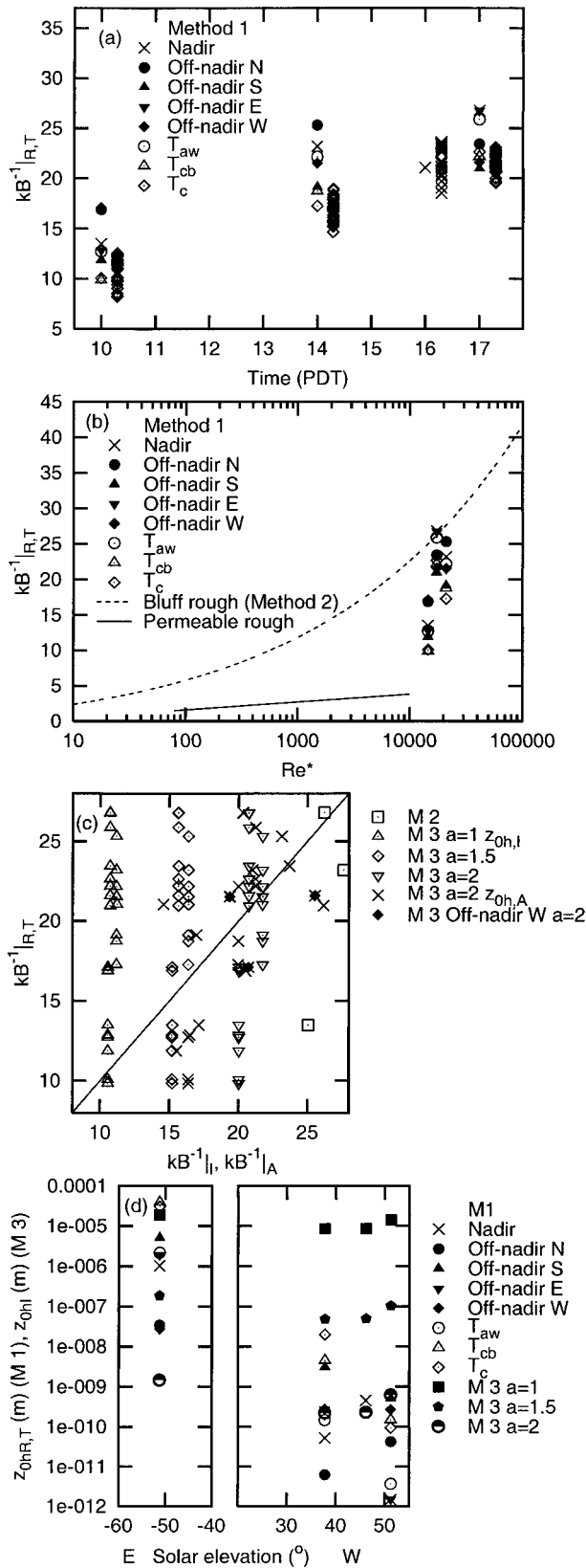
2) DERIVED COEFFICIENTS

Calculation of kB^{-1} was performed using three methods.

- 1) Method 1 ($kB^{-1}|_{R,T}$). Eq. (3) is used with $r_h = r_{am} + r_t$, and an explicit r_b in (1) is neglected. This approach is the most commonly used method (Stewart et al. 1994) that provides a direct back-calculated value.
- 2) Method 2 ($kB^{-1}|_{B82}$). Here z_{0hB82} is determined from (7) proposed by Brutsaert (1982) for bluff-rough surfaces.
- 3) Method 3 ($kB^{-1}|_I, kB^{-1}|_A$). Here $z_{0h,I}$ is determined for the isothermal case using (8), and $z_{0h,A}$ for the anisothermal case is determined using (9).

When method 1 is used, the values of $kB^{-1}|_{R,T}$ range from 10 to 27 (Fig. 8a) and clearly depend on the surface temperatures used. In general, the values calculated with nadir and off-nadir surface temperatures are higher than those that use the complete temperature values. A diurnal pattern is evident in the $kB^{-1}|_{R,T}$ values calculated, similar to that observed elsewhere [for a review see Verhoef et al. (1997)]. Higher values occur in the afternoon, generally rising later in the day (Fig. 8a). The smaller $z_{0h,R,T}$ (larger $kB^{-1}|_{R,T}$) values are associated with the largest ($T_R - T_a$) values but not the largest Q_H .

For the nadir thermal imagery (without consideration



of wall temperatures), $kB^{-1}|_{R,T}$ values are mostly in the range 13–27. The use of T_c reduces $kB^{-1}|_{R,T}$ by 3–6. Values derived from off-nadir directional temperatures span a wide range in accordance with the variability of surface temperature as seen in the various view directions. The use of the off-nadir temperature in the direction of the most shaded facet provides $kB^{-1}|_{R,T}$ values that are approximately the same as the T_c -based estimates. This result is in accordance with the similarity between the surface temperatures obtained using these two methods (Voogt and Oke 1997). This use of off-nadir temperatures to estimate the overall surface temperature is similar to the oblique measurements recommended by BS96. The variation in the values of $kB^{-1}|_{R,T}$ using T_c or nadir temperatures when the source areas are rotated about the tower position is 4–5 (Fig. 8a), with the value from the actual wind direction being within ± 1 standard deviation in all cases except at 17 h, the time period with the smallest standard deviation. This result suggests that the range of values that would be obtained from the general area around the tower would be within the other sampling error (< 1.5).

The $kB^{-1}|_{R,T}$ values reported here for the light industrial site are large relative to those determined for natural or agricultural surfaces. Most reported values of kB^{-1} , derived for vegetated surfaces, range from 1 to 10. A frequently cited value for natural surfaces is 2 (see, e.g., Stewart et al. 1994; Verhoef et al. 1997). Methods 2 and 3 provide an independent assessment of the appropriate size of kB^{-1} . Using Method 2, $kB^{-1}|_{BS2}$ is simply a function of Re^* , so the data plot on to the bluff rough curve from Brutsart (1982) (Fig. 8b). For comparison purposes, the permeable rough curve from Stewart et al. (1994) also is included. The $kB^{-1}|_{BS2}$ values of 25–27 obtained from (8) are at the high end of those obtained from Method 1 (Fig. 8b). However, they are more reasonable than those from the permeable rough curve. Using Method 3 (BS96), it is possible to begin to address the issue of the effect of the combination of surface and sensor angle geometry, which changes as the solar zenith angle varies through the day. As the sun rises, the

FIG. 8. (a) $kB^{-1}|_{R,T}$ values through time (for days 228 and 237) derived using different surface temperatures. The surface atmospheric meteorological variables correspond to the PDT hour they are plotted against. The values that are offset slightly against the hour are calculated using source areas that are rotated at 10° intervals around the tower and superimposed on the thermal imagery. (b) Method-1 $kB^{-1}|_{R,T}$ values superimposed on the bluff-rough curve of Brutsart (1982) (method 2) and the permeable rough curve of Stewart et al. (1994) against Re^* . (c) Comparison of kB^{-1} values determined by various methods against the method-1 values. The values calculated when T_r is the off-nadir west-facing data are shown explicitly: (i) method 2; (ii) method-3 results with three isothermal values ($kB^{-1}|_i$) using $a = 1, 1.5$, and 2; (iii) complete method-3 values ($kB^{-1}|_A$) with $a = 2$. (d) The $z_{ohr,T}$ values determined from method 1 and $z_{ohr,i}$ method 3 against solar elevation (negative values indicate east solar azimuth; positive values are west). Method 3 is the isothermal values determined with $a = 1, 1.5$, and 2.

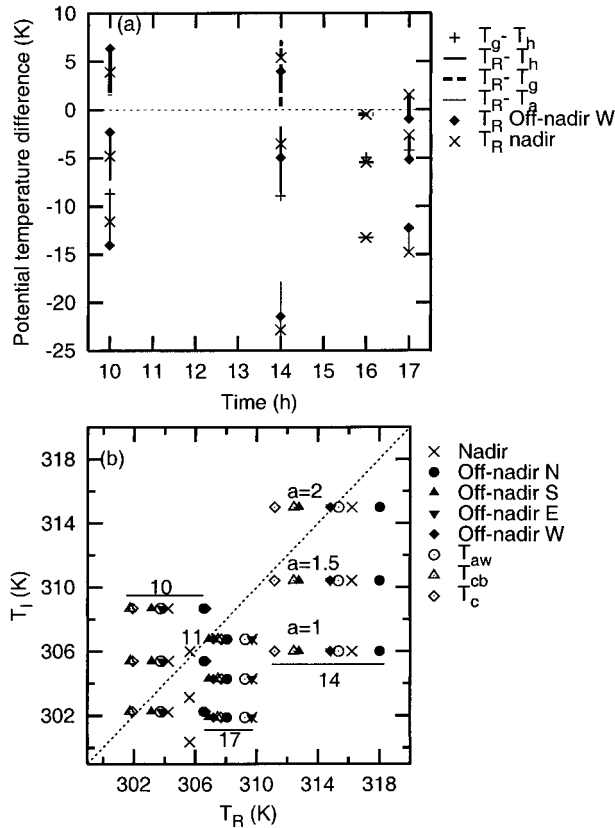


FIG. 9. (a) Temperature differences through time. (b) Isothermal surface temperature T_I calculated from method 3 against the radiative surface temperature T_R . Symbols indicate T_R method. The time of the observations is indicated by the horizontal lines. The vertical order of the data is consistent, between time periods, for the three a values used as shown for the 1400 data.

solar radiation penetrates deeper into the canopy (urban canyon), and the surface temperature increases. In the urban environment, because of the bluff-body nature of the roughness elements, there is a strong directional dependence (Fig. 4 and Fig. 5) in this heating. However, in this industrial/commercial area with very little vegetation, we do not see the situation that others have observed in which the bottom surface temperature exceeds the temperatures at the top of the canopy (Fig. 9a). This disparity is because the upper layer, in this case roofs of buildings, is not transpiring. Therefore, it continues to heat up through the day (Fig. 9a). In addition, although the top layers of the canopy are where most of the turbulent exchange takes place (BS96), in this environment the vertical components of the canopy (walls) also are important. The temperature difference between the roof (T_h) and the ground (T_g) decreases through the day (Fig. 9a), whereas $T_R - T_a$ has more of a parabolic diurnal trend, with the maximum in the middle of the day. Throughout the day, $T_R - T_h$ is negative, indicating that the roof temperature is much larger than the composite surface temperature (irrespective of method used to determine T_R). The size of the differ-

ence, however, decreases through the day. The difference between T_R and T_g is positive in the morning, but, by the late afternoon, with most methods it also is negative (Fig. 9a).

When $z_{ohR,T}$ is calculated from (3) and plotted against solar elevation (Fig. 8d), we find the following:

- 1) With use of T_{nadir} , the afternoon data show a similar pattern to BS96 (their Fig. 3) with $z_{ohR,T}$ decreasing with increasing solar elevation. However, the morning value of $z_{ohR,T}$ (at a zenith angle of 51°) is the largest (based on BS96 it would be expected to be of a similar size to that obtained late in the afternoon).
- 2) The off-nadir west-facing sensor (with a view angle of 45°) shows the least variability with solar elevation. This result suggests that back-calculated values should be the least biased by solar elevation.
- 3) The off-nadir north-facing sensor is the only view angle that shows an increase in $z_{ohR,T}$ in the afternoon with increasing solar elevation; all others show a decrease.

We can use the BS96 method as expressed in (8) to determine the isothermal $z_{oh,I}$ value, which should be independent of solar elevation and instrument geometry used to determine T_R . To use this method, a value needs to be assigned to a (all other terms are assigned values as outlined in section 2a). The present environment is extremely sparse in terms of vegetation but not in terms of roughness elements. The surface, however, is not densely covered by roughness elements. Based on this fact, a values of 1, 1.5, and 2 were assigned (from sparse to more dense canopy), which results in $z_{oh,I}$ values of 10^{-5} , 10^{-7} , and 10^{-9} m and $kB^{-1}|_I$ values of 11, 16, and 21, respectively (Fig. 8c). These values fall in the general range of the $kB^{-1}|_{R,T}$ values (Fig. 8c).

It then is possible to determine the isothermal surface temperature (T_I) that would produce the observed Q_H in (2) with $z_{oh,I}$ used in (1). Figure 9b shows the relation between T_I and T_R stratified by the a value assigned and by the method used to determine T_R . The ideal method to determine T_R is the one most consistent with T_I . This reasoning also indicates which $z_{oh,I}$ value is the most appropriate. Based on the mean differences and the mean absolute differences (Table 2), it is likely that the most appropriate value for a is 2, and the T_R method that most closely follows T_I is the off-nadir sensor that is west facing. If we relax the assessment to the mean difference $(\overline{T_I - T_R})$, then nadir, off-nadir north facing, and T_{aw} all have mean values that are, on average, less than 1°C different (but with std dev that are larger than 2.5°C).

The time period when the west-facing off-nadir radiometric surface temperature is most different from T_I is at 10 h (Fig. 9b). Therefore, it is likely that the kB^{-1} value at 10 h (Fig. 8a) probably is too low and the appropriate value for this environment is closer to that at 14 and 17 h; for $kB^{-1}|_{R,T}$ this value is 24, and from

TABLE 2. Differences between isothermal temperature and surface temperature (determined by a range of methods) (K). The values are the average (and standard deviation σ) of absolute differences ($|T_I - T_R|$) and the average (and standard deviation) difference ($\overline{T_I - T_R}$).

<i>a</i>	Statistic	<i>T_R</i> method						<i>T_{aw}</i>	<i>T_{cb}</i>	<i>T_c</i>	Average of all <i>T_R</i> methods
		Off-nadir									
		Nadir	N	S	E	W					
1	$ T_I - T_R $	6.32	7.49	4.21	6.05	6.17	6.05	4.16	3.76	5.56	
	$\sigma_{ T_I - T_R }$	3.52	4.02	3.00	3.92	2.30	4.09	3.20	2.99	3.15	
	$\overline{T_I - T_R}$	-6.32	-7.49	-4.21	-6.05	-6.17	-6.05	-3.83	-3.54	-5.49	
	$\sigma_{\overline{T_I - T_R}}$	3.52	4.02	3.00	3.92	2.30	4.09	3.77	3.36	3.27	
1.5	$ T_I - T_R $	3.72	4.18	2.39	3.80	2.86	3.86	2.94	2.54	3.30	
	$\sigma_{ T_I - T_R }$	2.25	3.25	0.17	1.98	1.54	1.89	0.84	1.55	1.73	
	$\overline{T_I - T_R}$	-3.14	-4.18	-0.89	-2.74	-2.86	-2.74	-0.52	-0.23	-2.20	
	$\sigma_{\overline{T_I - T_R}}$	3.22	3.25	2.73	3.78	1.54	3.83	3.65	3.46	3.06	
2	$ T_I - T_R $	2.24	2.16	2.62	2.66	0.86	2.60	3.39	3.83	2.53	
	$\sigma_{ T_I - T_R }$	1.82	0.86	2.74	2.36	0.98	2.31	3.20	2.92	2.08	
	$\overline{T_I - T_R}$	0.16	-0.73	2.56	0.71	0.59	0.71	2.93	3.22	1.23	
	$\sigma_{\overline{T_I - T_R}}$	3.16	2.63	2.83	3.93	1.25	3.84	3.82	3.87	3.08	
Average	$ T_I - T_R $	4.10	4.61	3.07	4.17	3.30	4.17	3.50	3.38	3.80	
Average	$\sigma_{ T_I - T_R }$	2.96	3.51	2.21	2.91	2.75	2.95	2.36	2.32	2.70	
Average	$\overline{T_I - T_R}$	-3.10	-4.13	-0.85	-2.70	-2.81	-2.69	-0.47	-0.18	-2.16	
Average	$\sigma_{\overline{T_I - T_R}}$	4.07	4.12	3.83	4.46	3.30	4.48	4.37	4.26	4.15	

$kB^{-1}|_I$ it is 21. These values correspond to $z_{ohR,T}$ of 7.5×10^{-11} and $z_{oh,I}$ of 4.2×10^{-10} m, respectively.

With use of (12) to determine the weighting factor w , the BS96 anisothermal $z_{oh,A}$ can be determined from (9). The results, shown in Fig. 8c, have a range similar to the $kB^{-1}|_{R,T}$ values.

The bulk radiative heat exchange coefficient C_{HR} ranges in size from 1.43×10^{-3} to 3.38×10^{-3} (Fig. 10a). When compared with C_{HR} as in (14), the coefficient a_{SM} is calculated as 0.111. This value compares favorably with the value Sun and Mahrt (1995b) derived for their data. However, it is important to note that the data reported here are for a much smaller range of conditions than those considered by Sun and Mahrt (1995b). Thus, the full extent of variability in this environment is not documented.

The radiometric roughness lengths for heat ($z_{ohR,T}$) are extremely small, ranging from 10^{-4} to 10^{-12} m; those $z_{oh,I}$ predicted by (8) are on the order of 10^{-9} m (Fig. 8d). This result suggests that similarity theory is predicting physically unrealistic values to compensate for the inadequacy of the stability dependence of the exchange coefficient or aerodynamic resistance [as documented previously by Sun and Mahrt (1995b)]. These small values have been found also by others, for example, Sugita and Brutsaert (1990) and Malhi (1996). The values determined here are likely to be close to the extreme because of the lack of vegetation at the site.

When the relation between $z_{ohR,T}$ and $-\Delta T/T_*$ is analyzed, after Sun and Mahrt (1995b) [(12)], the coefficients are found to be $c_1 = 3.22$ and $c_2 = -0.40$ (Figure 10b). These values are similar to those derived by Sun and Mahrt (1995b), showing consistency, once again, with other environments.

3) MODELED Q_H

It clearly is inappropriate to use the back-calculated $kB^{-1}|_{R,T}$ values to evaluate the ability to calculate Q_H , and insufficient data exist to evaluate independently the performance of the Q_H model. Thus, our approach here is to investigate the implications of assigning particular $kB^{-1}|_{R,T}$ values on modeled Q_H [using (3) and r_T from (6)]. This approach is of more general relevance, because those wishing to undertake this kind of modeling in urban environments in situations where measured Q_H is not available will likely select just one, or a limited range, of $kB^{-1}|_{R,T}$ values. Our approach is to assign a range of $kB^{-1}|_{R,T}$ values (2–60) and then to determine the average absolute difference between the observed and the modeled fluxes ($|\Delta Q_H| = |\overline{Q_{Hmeas}} - \overline{Q_{Hmod}}|$). The data used are for the three flights on day 228 (1000, 1400, and 1700 PDT) and the one flight on day 237 (1600 PDT) (indicated in Table 1). The modeled results are compared with the measured Q_H for the closest hour of observations. Note that all of the measurements will have errors that would result in different values. These errors are not considered here; others already have addressed this issue (see, e.g., Verhoef et al. 1997).

First, the effect of the method to determine bulk surface temperatures is considered (Fig. 11a). Day 237 only has nadir temperatures, thus for all other methods only the average of the three flights on day 228 is presented. The lowest overall $|\Delta Q_H|$ values ($< 8 \text{ W m}^{-2}$) were obtained using the west-facing off-nadir method source area temperature, with a kB^{-1} of 21 (Fig. 11a). The second-lowest minimum $|\Delta Q_H|$ values are from the north-facing off-nadir method; for $kB^{-1}|_{R,T}$ of 23–26, $|\Delta Q_H| < 15 \text{ W m}^{-2}$. The minimum $|\Delta Q_H|$ overall occur

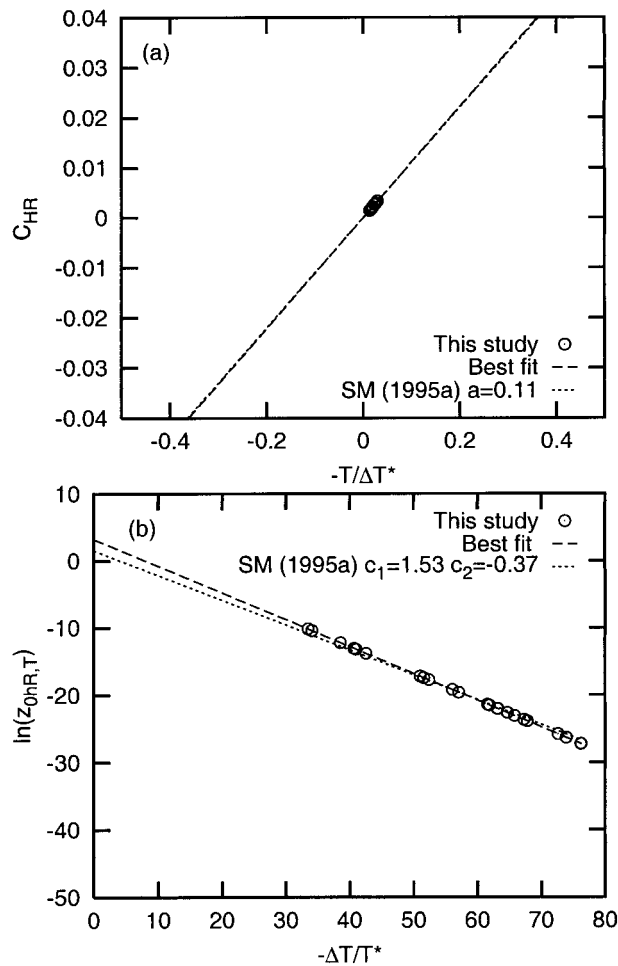


FIG. 10. (a) The radiometric exchange coefficient C_{HR} as a function of $-T^*/\Delta T$. Graph plotted with the same axes as used in Sun and Mahrt (1995b). Data from this study and derived best-fit line ($a_{SM} = 0.111$ with $n = 25$, using the range of surface temperature data) are shown with the Sun and Mahrt (1995b) overall best fit. (b) Radiometric roughness length for heat versus $-T^*/\Delta T$. Data from this study and derived best-fit line ($c_1 = 3.22$ and $c_2 = -0.400$ with $n = 25$), using the range of surface temperature data, are shown with the Sun and Mahrt (1995b) fit.

between $kB^{-1}|_{R,T}$ of 17 (for T_c) and 25 (off-nadir north facing). The choice of appropriate $kB^{-1}|_{R,T}$ value, that is, the one that minimizes the overall difference between measured and modeled heat fluxes, is sensitive to the off-nadir view direction of the surface. This result is consistent with the findings of BS96. Generally, the nadir and off-nadir results have a lower overall difference with measured data than those modeled using a pixel-by-pixel approach (T_{cb} , T_c). The largest difference is obtained using T_c (20.1 W m^{-2}).

If we ignore the method to determine T_R and just average the results of all methods together and examine variations through the course of the day, interesting patterns emerge (Fig. 11b). As noted earlier, based on the discussion of Fig. 8a, a diurnal trend in $kB^{-1}|_{R,T}$ is evident. The difference $|\Delta Q_H|$ is minimized at $kB^{-1}|_{R,T}$ of

13 for the first flight, and at 22–23 for flights 2 and 3. The afternoon data on day 237 are very similar, although not identical, to those on day 228. The smaller $|\Delta Q_H|$ on this day (Fig. 11b,c) is because there are only nadir T_R data. If we consider results for just one temperature method, namely, the nadir method T_R , the minimum $|\Delta Q_H|$ deviations are all less than 3 W m^{-2} (Fig. 11c). Thus, the difference in results between times (Fig. 11b) is greater than that between methods (Fig. 11a). This result is supported when we consider all of the methods but only on day 228. It also is notable, at the later period (228/17), that the range of $kB^{-1}|_{R,T}$ values with a $|\Delta Q_H|$ value of less than 10 W m^{-2} becomes larger. This result implies that the effect of selecting a slightly different $kB^{-1}|_{R,T}$ value is less for any of the temperature methods at this time.

Figure 11d summarizes the results across all times and methods and illustrates the relative error in Q_H for a given $kB^{-1}|_{R,T}$ ($|\Delta Q_H|/Q_{H,max}$). The lowest fractional error ($<18\%$) occurs when $kB^{-1}|_{R,T}$ is 21–23. However, the error variation around this range (Fig. 11d) is small; $kB^{-1}|_{R,T}$ values from 19 to 24 all yield an error less than 20%. This result indicates that, if the general fluxes are of interest rather than specific values for a given time, the approach is fairly robust and insensitive to the exact $kB^{-1}|_{R,T}$ value selected. These values correspond well with those predicted using the BS96 $kB^{-1}|_l$ with a equal to 2 (Fig. 8c, 20–22).

We can consider the implications of the exact area that is used to determine T_R . For the four flights, the area for which the remotely sensed data were collected is large enough to sample a series of different directions (source areas) at 10° intervals around the tower (228/10: 35 directions, 228/14: 36, 228/17: 36, and 237/16: 25). The calculated source area is placed over the nadir thermal composite image, and the temperatures are weighted by the source weight distribution function to determine a representative temperature for the flux source area. This temperature is used with the observed Q_H and T_a , which are assumed to represent reasonable local-scale estimates. Differences between measured and modeled fluxes $|\Delta Q_H|$ were less than 10 W m^{-2} at $kB^{-1}|_{R,T}$ of 11–12 for 228/10, at $kB^{-1}|_{R,T}$ of 17 for 228/14, at $kB^{-1}|_{R,T}$ of 19–24 for 228/17, and at a $kB^{-1}|_{R,T}$ of 21–24 for 237/16, when measured Q_H was 125 W m^{-2} . If, for each of the individual directions, we consider the minimum difference ($<10 \text{ W m}^{-2}$) between measured and modeled values, this difference occurs with a narrow range of $kB^{-1}|_{R,T}$ values [(T_c) 9–11, 17–18, 22–26, and (T_{nadir}) 22–25, for the four times, respectively]. Therefore, we can conclude that, for this study site under the conditions analyzed, the exact area that is sampled is not that critical; that is, the results spatially are very consistent.

Last, if $z_{0h,l}$ is used to model Q_H (using all T_R assignment methods or using the off-nadir west-facing T_R data), as expected, the ΔQ_H and $|\Delta Q_H|$ differences are minimized when a is 2 and are greatest when a is 1

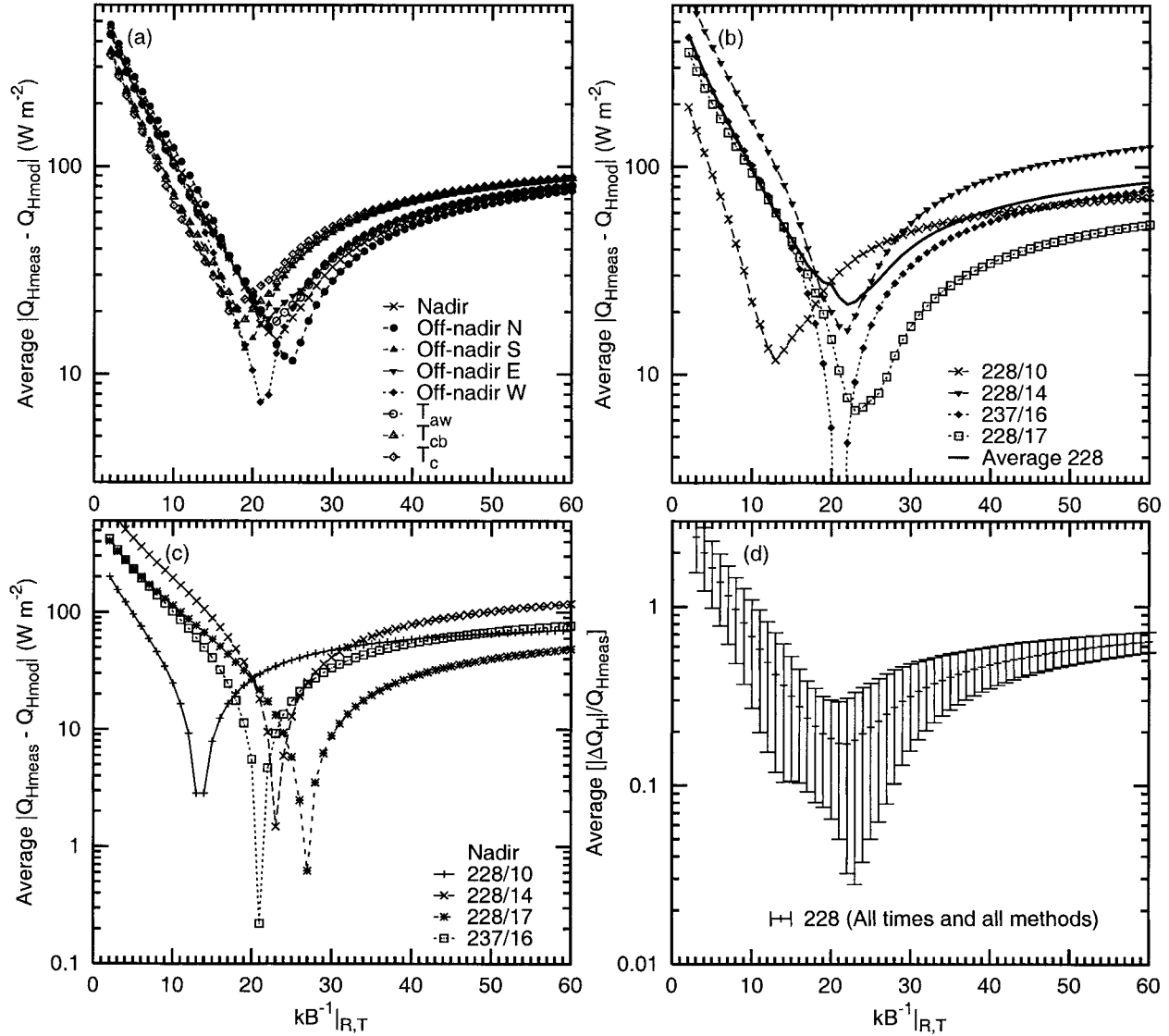


FIG. 11. Absolute difference between the observed and the modeled Q_H ($|\overline{\Delta Q_H}| = \overline{|Q_{Hmeas} - Q_{Hmod}|}$) for varying $kB^{-1}|_{R,T}$ values. (a) Bulk surface radiative temperature determined by the range of methods discussed in section 3e, results are the average for three flights on day 228, data for day 237 included in the nadir method; (b) results by time period averaged for the eight methods to determine the temperature; (c) bulk surface radiative temperature determined by nadir method for all time periods; (d) average (and standard deviation) difference between measured and modeled values for all flights and temperature methods for given $kB^{-1}|_{R,T}$ values.

TABLE 3. Differences between measured and modeled Q_H ($W m^{-2}$) using $z_{oh,l}$ for all T_R methods and for off-nadir west T_R .

		z_{oh}		
		$a = 1$	$a = 1.5$	$a = 2$
All T_R , $n = 26$	$\overline{\Delta Q_H}$	-79.4	-25.7	7.2
	$ \overline{\Delta Q_H} $	103.5	53.6	33.4
T_R (off-nadir west), $n = 3$	$\overline{\Delta Q_H}$	-85.5	-30.3	3.6
	$ \overline{\Delta Q_H} $	70.0	28.6	3.2

(Table 3). There is a reduction in $|\overline{\Delta Q_H}|$ in all cases when off-nadir west-facing data are used (although n is only 3). This result suggests that using a BS96 $z_{oh,l}$ value would generate reasonable results, but assigning the appropriate a value will have an effect on the size of the errors. To assign the appropriate parameter ahead of time requires additional studies of different urban areas.

c. Microscale variability

An alternative approach to model Q_H , proposed by Sun and Mahrt (1995a), uses temperature gradients and conductances for surfaces within the domain of interest.

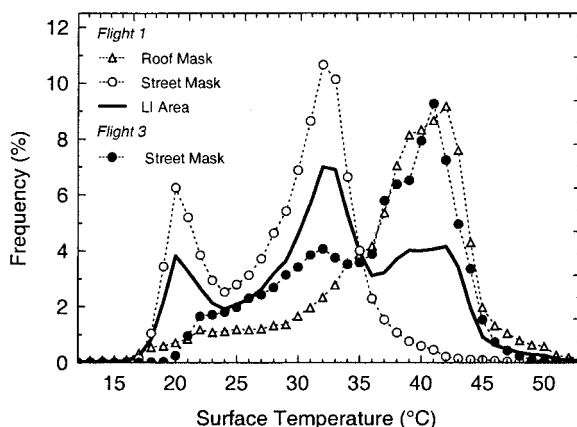


FIG. 12. Frequency distribution of surface temperatures extracted using the building database masks for streets, roofs, and the entire area for flight 1, and for the street mask from flight 3.

The relative simplicity of the study area and assessment of the temperature distribution allows a generalization of the surface into a limited number of components, which then can be used to assess this method. The surface fractions considered are plan surfaces of roof, sunlit street and shaded street, and each of the wall directions.

1) SURFACE TEMPERATURES

The urban surface is heterogeneous at small scales, with large variations in surface temperature occurring over short distances (Figs. 3 and 12). Frequency distributions of image temperature are multimodal in character. Peaks within the distribution are distinguished most strongly in the morning (Voogt and Oke 1998a) and can be related to surface type. Figure 12 illustrates the frequency distribution of plan surface temperatures for flight 1. Despite the wide range in surface temperature, the distributions suggest an underlying reduction of the surface to a few main components. The uppermost peak of the surface temperature distribution is related to roof temperature, the middle peak to open sunlit streets, and the lowest peak to fully shaded surfaces. The component temperature distributions are broadened somewhat by misregistration of pixels because of the simplified building outlines used, errors in compositing the thermal imagery, and very low emissivity surfaces. In general, the surface temperature in the shaded areas is only slightly warmer than the air temperature, espe-

cially prior to solar noon, whereas the sunlit areas are much warmer. Thus, the heat flux probably is dominated by the sunlit area.

Separation of the shaded and sunlit street surface temperatures was accomplished using a limiting temperature for shaded surfaces. This choice was made over a more independent calculation of shaded areas using the building database and solar geometry because of the simple three-dimensional structure represented by the building database. The disadvantage of the method is misclassification of shaded surfaces. This problem is most apparent following solar noon when hot surfaces with large heat capacities are now shaded yet exhibit relatively high surface temperatures in comparison with surfaces that have been shaded throughout the day, for example, east-facing wall temperatures (Fig. 4) and street temperatures (Fig. 12) in the afternoon. Despite this problem, temperature bounds for shaded surfaces, extracted from inspection of temperature distributions, yield qualitatively correct shading patterns when combined with the masks of roof and street surfaces. Misregistration of pixels because of low surface emissivity is minimized by first masking off building roofs, which are much more likely to exhibit low surface emissivity values.

The fraction of area that is sunlit (F_{sun}) and shaded (F_{sha}) varies through time (Table 4) and also depends on the source area size and position. This variation is caused by the change in both the vertical and the horizontal areas that are sunlit. In terms of the vertical components, clearly, east-facing walls are sunlit first and west-facing walls are the last to be sunlit. The shadows that are cast on the low-lying horizontal surfaces, primarily roads, change as the sun's position changes through the day. However, the roof area remains primarily sunlit throughout the daylight hours. The fractional significance of this is dependent on the height of the walls. In this area, in which there are large numbers of warehouse-type buildings, the wall area is less significant than if the site was a downtown area with taller buildings. The ratio of wall to complete area in the study site is 0.3, the ratio of roof to complete surface area is 0.3, and the remaining 0.4 is streets (open ground). The fractional roof area is also dependent upon the source area dimensions and position. Figure 13 shows some variability of fractional roof area as source area size increases, even at the scale of the calculated source areas for day 228. In addition, the calculated fraction can be

TABLE 4. Component surface temperatures and the fraction of the flux source area that they represent for 1992 yearday 228.

Day/hr	Temperature (K)							Fraction (%)						
	Wall facing				Road		Roof	Wall facing				Road		Roof
	N	E	W	S	Sun	Shade		N	E	W	S	Sun	Shade	
228/1000	292.78	304.51	292.51	299.47	302.44	291.81	309.02	8.5	7.2	7.1	8.2	7.6	31.1	30.3
228/1400	294.26	300.91	299.40	309.00	313.79	294.44	319.74	8.3	6.1	5.9	8.0	5.3	30.4	36.0
228/1700	296.02	298.12	308.79	303.65	311.12	297.27	312.34	8.1	6.1	5.8	8.1	7.6	28.6	35.7

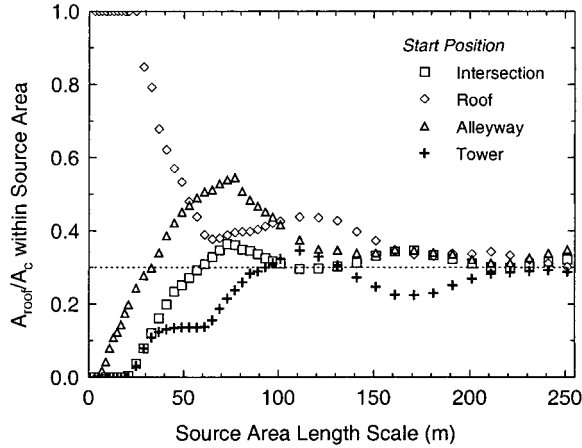


FIG. 13. Fraction of roof area to complete surface area within square “source areas” of a given size. The dashed line represents the value calculated for the building database domain corresponding to the composite image area.

sensitive to the center position of the source area, as indicated by the difference in the calculated fractions for different starting points that have the same source area.

2) VARIATION IN CONDUCTANCES/RESISTANCES BECAUSE OF SURFACE CHARACTERISTICS

Using the methods of Sun and Mahrt (1995a), the effect of the surface characteristics is considered (see section 2b), with the surface divided into sunlit (F_{sun}) and shaded (F_{sha}) fractions. The fractions vary with time (Tables 4 and 5), with F_{sun} increasing from 0.45 to 0.57 through the day. Five methods (reference numbers given in square brackets) were used to determine C_{HR} : [1] (1) with $z_{oh} = z_{om}$, [2] (1) with $z_{oh} = 0.1(z_{om})$, [3] Malhi

[1996, (30)] with $z_{oh} = z_{om}$, [4] Malhi [1996, (30)] with $z_{oh} = 0.1(z_{om})$, and [5] (1) with $z_{oh} = z_{oh,l}$ (with $a = 2$). The $z_{oh} = z_{om}$ assumption follows Sun and Mahrt’s assumption; the $z_{oh} = 0.1(z_{om})$ is a common a priori assumption for rough environments, based on Brutsaert (1982). Case 5 is based on the results presented in section 4b (2).

The component conductances and the aerodynamic surface temperatures T_0 , determined from (2), are given in Table 5 for each time period and case. We summarize the results as follows.

- (a) In cases 1–4, T_0 generally is similar in size to T_{sha} ; the differences between T_0 and T_{sun} are larger (10–23 K). The maximum $T_0 - T_a$ differences are less than 4 K (case 2).
- (b) In cases 1–4, T_0 is much smaller than for case 5.
- (c) In case 5, the $T_0 - T_a$ differences are 13–18 K, and $T_0 - T_{sha}$ differences are 11–19 K, with the larger $T_0 - T_a$ differences associated with larger $T_0 - T_{sha}$ differences.
- (d) In some situations the conductances become negative. In cases 1–4, these situations occur when T_0 is less than T_{sha} . However, in case 5, this situation occurs when T_0 is greater than T_{sun} (228/10).
- (e) Case 2 produces no negative conductances.
- (f) In cases 1–4, the shade conductance g_{sha} is larger than the sunlit conductance g_{sun} . The opposite is true for case 5.

The results of this work clearly fall into two groups: those with the larger z_{oh} values (cases 1–4), and case 5. In the first instance, the results are very different from Sun and Mahrt’s (1995a) study of a sunlit black spruce tree canopy and shaded ground at 1300 LST, in which T_0 was very similar to the treetop temperature. On the other hand, the case-5 results are similar both in terms

TABLE 5. Conductances determined for sunlit and shaded fractions of the surface (see section 2b). Methods used to determine C_{HR} are [1] (1) with $z_{oh} = z_{om}$, [2] (1) with $z_{oh} = 0.1(z_{om})$, [3] Malhi [1996, (30)] with $z_{oh} = z_{om}$, [4] Malhi [1996, (30)] with $z_{oh} = 0.1(z_{om})$, and [5] (1) with $z_{oh} = z_{oh,l}$ (with $a = 2$). Assumptions are surface partitioned into seven fractions: roof (f_r), north wall (f_n), east wall (f_e), south wall (f_s), west wall (f_w), sunlit street (f_{su}), and shaded street (f_{sh}).

Year/day/h	Assumptions, air and surface temperatures (K)	C_{HR} method	T_0 (K)	g_{sun} ($m\ s^{-1}$)	g_{sha} ($m\ s^{-1}$)	$\frac{g_{sun}}{C_{HR}U}$	$\frac{g_{sha}}{C_{HR}U}$	$\frac{g_{sun}}{g_{sha}}$
228/1000	$F_{sun} = f_e + f_r + f_{su}$ $T_a = 292.66$ $T_{sun} = 307.19$ $T_{sha} = 293.20$	1	295.07	0.0098	0.0520	0.2974	1.5767	0.1886
		2	296.64	0.0109	0.0275	0.5456	1.3729	0.3974
		3	293.07	-0.0041	0.3637	-0.0208	1.8379	-0.0113
		4	293.71	0.0062	0.1340	0.0806	1.7546	0.0459
		5	308.69	0.0122	-0.0010	2.4570	-0.1959	-12.5444
228/1400	$F_{sun} = f_s + f_r + f_{su}$ $T_a = 296.52$ $T_{sun} = 317.36$ $T_{sha} = 295.77$	1	296.51	-0.0038	0.1016	0.0704	1.9043	0.0370
		2	298.47	0.0084	0.0569	0.2541	1.7256	0.1473
		3	294.05	-0.0390	0.5166	-0.1608	2.1292	-0.0755
		4	294.97	-0.0078	0.2137	-0.0746	2.0453	-0.0365
		5	315.00	0.0141	0.0017	1.8059	0.2162	8.3576
228/1700	$F_{sun} = f_w + f_s + f_r + f_{su}$ $T_a = 294.89$ $T_{sun} = 310.16$ $T_{sha} = 297.16$	1	296.68	-0.0026	0.1043	-0.0617	2.4217	-0.0255
		2	297.80	0.0022	0.0509	0.0838	2.2267	0.0377
		3	295.27	-0.0503	0.5465	-0.2455	2.6678	-0.0920
		4	295.78	-0.0155	0.2234	-0.1788	2.5784	-0.0693
		5	308.14	0.0081	0.0044	1.2344	0.6740	1.8451

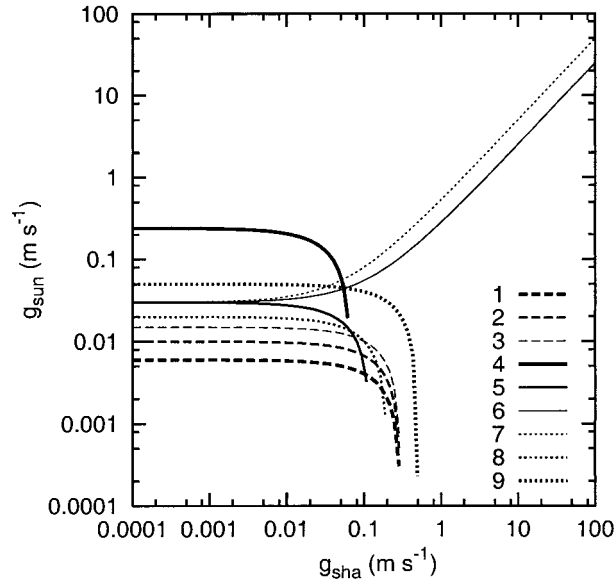


FIG. 14. Effect of changing the kinematic heat flux (H , $\text{m s}^{-1} \text{K}$), the size of the temperature gradients (ΔT_{sun} and ΔT_{sha} , K) and the fraction shaded ($F_{\text{sha}} = 1 - F_{\text{sun}}$) on g_{sun} as a function of g_{sha} . Input parameters for the sensitivity test of g_{sun} and g_{sha} :

Line	1	2	3	4	5	6	7	8	9
H ($\text{m s}^{-1} \text{K}$)	0.12	0.12	0.12	0.12	0.12	0.12	0.12	0.08	0.20
F_{sha}	0.2	0.2	0.2	0.9	0.2	0.2	0.2	0.2	0.2
$T_{\text{sun}} - T_a$ (K)	25	15	5	5	5	5	5	5	5
$T_{\text{sha}} - T_a$ (K)	2	2	2	2	5	-5	-10	2	2

of the relative temperature differences (large $T_{\text{sha}} - T_0$ and small $T_{\text{sun}} - T_0$) and the ratio of the two conductances ($g_{\text{sun}}/g_{\text{sha}}$), which for their study was on the order of 16. Here we can look also at two other time periods, in addition to the middle of the day. In the late afternoon, the ratio of the conductances has dropped to about 2. In the morning, the method predicts a negative g_{sha} value that clearly leads to a negative ratio, although the absolute magnitude is similar to that of the middle of the day.

To gain more general insight into the conditions that can yield negative conductances, a sensitivity test was conducted using

$$H = F_{\text{sun}}g_{\text{sun}}(T_{\text{sun}} - T_a) + F_{\text{sha}}g_{\text{sha}}(T_{\text{sha}} - T_a). \quad (24)$$

Given the constraint of (17), the effect of changing the kinematic heat flux H and the effect of the size of the temperature gradients ($\Delta T_{\text{sun}} = T_{\text{sun}} - T_a$ and $\Delta T_{\text{sha}} = T_{\text{sha}} - T_a$) on g_{sun} and g_{sha} are investigated (Fig. 14). Only positive conductance values (physically reasonable) are shown. From Fig. 14, it is clear that, for conditions around g_{sha} of $0.01\text{--}1 \text{ m s}^{-1}$, it is possible to have physically unreasonable g_{sun} values with small changes in ambient conditions. These results suggest that there are wide ranges of conditions under which this method will fail, not just limited to those we en-

countered in this study. If ΔT_{sha} becomes negative, then both g_{sun} and g_{sha} increase in size.

As noted earlier (section 4a), the Q_H values were low on day 228. If the entire measurement period ensemble Q_H values are used in the calculations instead (which also influences the C_H values used) with all other inputs held constant, $g_{\text{sun}}/g_{\text{sha}}$ becomes slightly larger in the afternoon. However, g_{sun} values remain negative for cases 1, 3, and 4, and g_{sha} is negative for case 5.

From this kind of analysis, it clearly is important to have a reasonable estimate of z_{oh} . The isothermal value from BS96 seems to provide a good first approximation. However, the results do show that there are problems with the method at certain times of the day. These problems may be related to the definition of the fractions of the surface. For example, the case-5 negative value could have been avoided if the sunlit fraction had been defined as only the roof (Tables 3 and 4).

5. Conclusions

Bulk and microscale methods of estimating surface sensible heat flux have been examined for an urban area almost devoid of vegetation and characterized by rectangular buildings that act as bluff-rough elements. The explicit recognition of temperatures of vertical surfaces often undersampled by nadir remote sensors is included in this analysis. This inclusion has the effect of reducing the surface temperature by 2–7 K during the daytime observation period.

For this environment, a reasonable estimate for $kB^{-1}|_{R,T}$ appears to be about 20–27, which is larger than those observed over vegetated and agricultural surfaces and suggests extremely small z_{oh} values. This range represents the results obtained by three independent methods. The values determined for the bluff-rough curve (Brutsaert 1982) provide the largest values. At the lower end are those values predicted by the isothermal method of Brutsaert and Sugita (1996). Intermediate values (21–23) are obtained from the back-calculation method. From the analysis presented in Fig. 11d, the implications for the likely size of error in Q_H can be determined. From this analysis, we conclude that, for this kind of urban environment with little vegetation, an appropriate kB^{-1} value could be obtained by using the Brutsaert (1982) method as expressed in (7) or the isothermal method of Brutsaert and Sugita (1996) as expressed in (8). However, the assessment of the appropriate a value for (8) (Brutsaert and Sugita 1996) in this environment requires further investigation.

The exact $kB^{-1}|_{R,T}$ value varies, depending on the method used to determine the surface temperatures. The off-nadir west-facing temperature data provided the lowest error in modeled Q_H in this study. Generally, the nadir and off-nadir results have a lower overall difference with measured data than those modeled using a pixel-by-pixel approach (T_{aw} , T_{cb} , T_c). There is a very

small difference between methods to determine wall temperatures.

Diurnal variations in $kB^{-1}|_{R,T}$ are evident. However, the suggestion by Brutsaert and Sugita (1996) that these variations may be due in part to solar elevation also appears to be a reasonable explanation. Solar geometry plays an important role in creating urban local- and microscale climates. This is particularly the case at this light industrial site because of the large size of the roughness elements, the orderly location of the elements relative to the solar path, the large building surface area with large thermal inertia, and low evaporative ability. Consequently, this site provides an opportunity to consider the BS96 suggestion that the variability in z_{oh} may be due to the interaction of solar and surface geometry. In this study, the combined role of geometry is considered in three different ways, as follows.

- 1) *Bulk surface temperature:* A series of different combinations of solar and surface geometries are obtained through use of different bulk surface temperature representations. Representations include a range of directly observable radiometric temperatures from nadir and off-nadir view angles as well as calculated composite temperatures that incorporate all surfaces.
- 2) *Partitioning of the surface by position:* The surface is divided, and temperatures are determined for the ground level and z_h level. In an urban area (without trees), the z_h level is the roof. This representation neglects the building walls. In a vegetated area, a temperature determined for z_h will inherently involve some sort of integrated response of the top layers of the canopy, given the porous nature of vegetative canopies and the view angle of the sensor. The BS96 anisothermal model partitions the surface in this way.
- 3) *Partitioning of the surface by radiative condition:* In this case, all aspects of the surface area are taken into account but relative position is not. Thus, the sunlit fraction constitutes roof, some ground, and some wall areas. The actual areas and fractions vary through time and have different thermal histories, which, because of the thermal inertia, can be significant. This type of partitioning is used in our application of the Sun and Mahrt microscale variability method.

The coefficients proposed for relations with $-T_*/\Delta T$ by Sun and Mahrt (1995b) from a range of vegetated surfaces are shown to agree well with our results for a dry urban environment. This agreement suggests that these empirical relations may hold across a wider range of conditions.

In this environment, when the surface is subdivided into sunlit and shaded fractions of the surface, the estimates of subcomponent conductances do not produce meaningful results throughout the day. We attribute this to the fact that, during the later portion of the day, there are surfaces (both horizontal and vertical) that are no

longer sunlit but are still very warm. Thus, the anisothermal behavior suggested by BS96 and identified here in the bulk values may explain also the inability to model the microscale conductances throughout the day. Clearly, this result has implications in other environments where strong thermal inertia may be evident. We also conclude that the initial assumption of the size of z_{oh} is important for this method. In this environment with large bluff bodies, the initial assumption of Sun and Mahrt (1995a) is not appropriate.

Our results show that first-order estimates of heat fluxes can be estimated using this approach, but careful attention needs to be directed to the method by which surface temperatures are defined and determined and to the diurnal variability of model parameters, notably $kB^{-1}|_{R,T}$. Clearly more research in more complex urban environments is needed.

Acknowledgments. We thank our many field assistants, Dr. T. R. Oke for his advice on many aspects of this work, and Dr. H. P. Schmid for assistance with FSAM. We also thank the three anonymous reviewers for their useful comments and suggestions on an earlier version of the manuscript. This research was funded by NSERC (Voogt) and a USDA Forest Service cooperative grant (Grimmond).

APPENDIX

List of Symbols

Note: all temperatures T are potential temperatures.

A_c	complete surface area
A_i	area of surface type i
A_p	plan (horizontal) surface area
A_{roof}	roof area
$A_{\text{st(sha)}}$	shaded street area
A_w	wall area
a	extinction coefficient in the exponential shear stress profile
a_{SM}	coefficient for C_{HR} relationship from Sun and Mahrt (1995b)
B^{-1}	dimensionless parameter = $r_b u_* = \ln(z_{om}/z_{oh})/k$
$B^{-1} _{R,T}$	dimensionless parameter = $r_T u_* = \ln(z_{om}/z_{ohR,T})/k$
b	extinction coefficient for the vertical canopy temperature profile
C_2	coefficient defined by (10) and used in (8) and (9)
C_a	volumetric heat capacity of air
C_D	bulk drag coefficient for momentum
C_H	bulk exchange coefficient for heat
C_{HR}	bulk radiometric exchange coefficient for heat
Ct_f	transfer coefficient for use with (8) and (9)
C_L	fitting parameter for Ct_f
c_1	coefficient for use with (16)
c_2	coefficient for use with (16)

c_p	specific heat capacity	T_{sha}	radiometric shaded surface temperature
F_{sha}	total shaded fraction of the surface	T_*	temperature scale = $-H/u_*$
F_{sun}	total sunlit fraction of the surface	U	mean horizontal wind speed
f_i	fractional area of coverage by surface type i	u_*	friction velocity
g	bulk surface heat conductance	w	weighting fraction for surface temperature
g_i	surface heat conductance for surface type i	z_{0h}	roughness length for heat
\hat{g}_i	normalized surface heat conductance for surface type i	$z_{0h,B82}$	roughness length for heat, calculated using Brutsaert (1982) method [Eq. (7)]
g_{sha}	surface heat conductance for shaded surfaces	$z_{0h,A}$	anisothermal scalar roughness length
g_{sun}	surface heat conductance for sunlit surfaces	$z_{0h,I}$	isothermal roughness length for heat
H	kinematic heat flux	$z_{0h,R,T}$	radiometric roughness length for heat, calculated using r_f
k	von Kármán constant	z_{0m}	roughness length for momentum
kB^{-1}	the natural logarithm of the ratio of roughness length of heat to momentum	z_d	zero-plane displacement length
$kB^{-1} _{B82}$	kB^{-1} derived using Brutsaert (1982) [Eq. (7)]	z_h	height of the roughness elements
$kB^{-1} _{R,T}$	kB^{-1} derived using $z_{0h,R,T}$ (back-calculated value) [Eq. (3)]	z_s	sensor or measurement height
$kB^{-1} _I$	kB^{-1} derived using $z_{0h,I}$ (BS96 isothermal case) [Eq. (8)]	β	Bowen ratio
$kB^{-1} _A$	kB^{-1} derived using $z_{0h,A}$ (BS96 anisothermal case) [Eq. (9)]	λ_c	complete aspect ratio = A_c/A_p
L	Obukhov length	ν	kinematic molecular viscosity
m	fitting parameter in Ct_f	ρ	density of air
N	number count	σ	standard deviation
n	fitting parameter in Ct_f	σ_v	standard deviation of the crosswind velocity
Pr	Prandtl number	Ψ_H	stability correction for heat
Q^*	net allwave radiative flux	Ψ_M	stability correction for momentum
Q_E	latent heat flux		
Q_H	sensible heat flux		
$ \Delta Q_H $	average absolute difference between observed and modeled sensible heat fluxes		
ΔQ_S	storage heat flux		
Re^*	roughness Reynolds number		
r_2	coefficient for BS96		
r_{ah}	aerodynamic resistance to heat transfer between the height $z_d + z_{0h}$ and z_s		
r_{am}	aerodynamic resistance for momentum		
r_b	bulk aerodynamic excess resistance		
r_h	aerodynamic resistance to heat		
r_r	excess resistance from different heat source and momentum sink locations		
r_T	excess resistance between z_{0m} and the surface		
T_0	aerodynamic surface temperature		
T_a	air temperature		
T_{aw}	area-weighted radiometric surface temperature for an image pixel		
T_c	complete (or area weighted) radiometric surface temperature for a specified spatial domain		
T_{cb}	complete (radiometric) temperature for an individual building		
T_g	surface temperature near the ground		
T_h	surface temperature near z_h		
T_i	temperature of surface element i within a pixel		
T_I	isothermal surface temperature		
T_{nadir}	nadir (directional) radiometric temperature		
T_R	radiometric surface temperature		
T_{sun}	radiometric sunlit surface temperature		

REFERENCES

- Arnfield, A. J., 1982: An approach to the estimation of the surface radiative properties and radiation budgets of cities. *Phys. Geogr.*, **3**, 97–122.
- Brutsaert, W., 1979: Heat and mass transfer to and from surfaces with dense vegetation or similar permeable roughness. *Bound.-Layer Meteor.*, **16**, 365–388.
- , 1982: *Evaporation into the Atmosphere*. D. Reidel, 229 pp.
- , and M. Sugita, 1996: Sensible heat transfer parameterization for surfaces with anisothermal dense vegetation. *J. Atmos. Sci.*, **53**, 209–216.
- Byrnes, A. E., and J. R. Schott, 1986: Correction of thermal imagery for atmospheric effects using aircraft measurement and atmospheric modeling techniques. *Appl. Opt.*, **25**, 2563–2570.
- Desjardins, R., J. Gray, and F. Bonn, 1990: Atmospheric corrections for remotely sensed thermal data in a cool humid temperate zone. *Int. J. Remote Sens.*, **11**, 1369–1389.
- Dyer, A. J., 1974: A review of flux–profile relationships. *Bound.-Layer Meteor.*, **7**, 363–372.
- Grimmond, C. S. B., and H. A. Cleugh, 1994: A simple method to determine Obukhov lengths for suburban areas. *J. Appl. Meteor.*, **33**, 435–440.
- , and T. R. Oke, 1999a: Aerodynamic properties of urban areas derived from analysis of surface form. *J. Appl. Meteor.*, **38**, 1262–1292.
- , and ———, 1999b: Heat storage in urban areas: Local-scale observations and evaluation of a simple model. *J. Appl. Meteor.*, **38**, 922–940.
- Högström, U., 1988: Non-dimensional wind and temperature profiles in the atmospheric surface layer: A re-evaluation. *Bound.-Layer Meteor.*, **42**, 55–78.
- Huband, N. D. S., and J. L. Monteith, 1986: Radiative surface temperature and energy balance of a wheat canopy. I. Comparison of radiative and aerodynamic temperatures. *Bound.-Layer Meteor.*, **36**, 1–17.
- Kneizys, F. X., E. P. Shettle, L. W. Abreu, J. H. Chetwynd Jr., G. P. Anderson, W. O. Gallery, J. E. A. Selby, and S. A. Clough, 1988: User's guide to LOWTRAN 7. Air Force Geophysics Laboratory

- Rep. AFGL-TR-88-0177, 137 pp. [Available from Air Force Geophysical Laboratory, Hanscom Air Force Base, MA 01731.]
- Kubota, A., and M. Sugita, 1994: Radiometrically determined skin temperature and scalar roughness to estimate surface heat flux. Part I: Parameterization of radiometric scalar roughness. *Bound.-Layer Meteor.*, **69**, 397–416.
- Kustas, W. P., B. J. Choudhury, M. S. Moran, R. J. Reginato, R. D. Jackson, L. W. Gay, and H. L. Weaver, 1989: Determination of sensible heat flux over sparse canopy using thermal infrared data. *Agric. For. Meteor.*, **44**, 197–216.
- Lacis, A. A., and V. Oinas, 1991: A description of the correlated k distribution method for modeling nongray gaseous absorption, thermal emission, and multiple scattering in vertically inhomogeneous atmospheres. *J. Geophys. Res.*, **96**, 9027–9063.
- Malhi, Y., 1996: The behaviour of the roughness length for temperature over heterogeneous surfaces. *Quart. J. Roy. Meteor. Soc.*, **122**, 1095–1125.
- Norman, J. M., M. Divakarla, and N. S. Goel, 1995: Algorithms for extracting information from remote thermal-IR observations of the earth's surface. *Remote Sens. Environ.*, **51**, 157–168.
- Owen, P. R., and W. R. Thomson, 1963: Heat transfer across rough surfaces. *J. Fluid Mech.*, **15**, 321–334.
- Paulson, C. A., 1970: The mathematical representation of wind speed and temperature profiles in the unstable atmospheric surface layer. *J. Appl. Meteor.*, **9**, 857–861.
- Prata, A. J., 1994: Land surface temperatures derived from the advanced very high resolution radiometer and the along-track scanning radiometer. 2: Experimental results and validation of AVHRR algorithms. *J. Geophys. Res.*, **99**, 13 025–13 058.
- Raupach, M. R., 1992: Drag and drag partition on rough surfaces. *Bound.-Layer Meteor.*, **60**, 375–395.
- , 1994: Simplified expressions for vegetation roughness length and zero-plane displacement as functions of canopy height and area index. *Bound.-Layer Meteor.*, **71**, 211–216.
- , 1995: Corrigenda. *Bound.-Layer Meteor.*, **76**, 303–304.
- Schmid, H. P., 1994: Source areas for scalars and scalar fluxes. *Bound.-Layer Meteor.*, **67**, 293–318.
- , 1997: Experimental design for flux measurements: Matching the scales of observations and fluxes. *Agric. For. Meteor.*, **87**, 179–200.
- , and T. R. Oke, 1992: Scaling North American urban climates by lines, lanes, and rows. *Geographical Snapshots of North America*, D. G. Janelle, Ed., Guilford Publications, 395–399.
- , and C. R. Lloyd, 1999: Spatial representativeness and the location bias of flux footprints over inhomogeneous areas. *Agric. For. Meteor.*, **93**, 195–209.
- Stewart, J. B., W. P. Kustas, K. S. Humes, W. D. Nichols, M. S. Moran, and H. A. R. de Bruin, 1994: Sensible heat flux–radiometric temperature relationship for eight semiarid areas. *J. Appl. Meteor.*, **33**, 1110–1117.
- Sugita, M., and W. Brutsaert, 1990: Regional fluxes from remotely sensed skin temperature and lower boundary layer measurements. *Water Resour. Res.*, **26**, 2937–2944.
- Sun, Y., and L. Mahrt, 1995a: Relationship of surface heat flux to microscale temperature fluctuations. *Bound.-Layer Meteor.*, **76**, 291–301.
- , and —, 1995b: Determination of surface fluxes from the surface radiative temperature. *J. Atmos. Sci.*, **52**, 1096–1106.
- Tanner, B. D., and J. P. Greene, 1989: Measurements of sensible heat and water vapor fluxes using eddy correlation methods. Final Rep. to U.S. Army Dugway Proving Grounds, DAAD 09-87-D-0088, 94 pp. [Available from Campbell Scientific, Inc., 815 West 1800 North, Logan, UT 84321-1784.]
- , E. Swiatek, and J. P. Greene, 1993: Density fluctuations and use of krypton hygrometers in surface flux measurements. *Management of Irrigation and Drainage Systems*, Park City, UT, Amer. Soc. Civil Eng., 945–952.
- Troufleau, D., J. P. Lhomme, B. Monteny, and A. Vidal, 1997: Sensible heat flux and radiometric surface temperature over sparse Sahelian vegetation. I. An experimental analysis of the kB^{-1} parameter. *J. Hydrol.*, **188–189**, 815–838.
- van Ulden, A. P., and A. A. M. Holtslag, 1985: Estimation of atmospheric boundary layer parameters for diffusion applications. *J. Climate Appl. Meteor.*, **24**, 1196–1207.
- Verhoef, A., H. A. R. de Bruin, and J. J. M. van den Hurk, 1997: Some practical notes on the parameter kB^{-1} for sparse vegetation. *J. Appl. Meteor.*, **36**, 560–572.
- Verma, S. B., 1989: Aerodynamic resistances to transfers of heat, mass and momentum. *Estimation of Areal Evapotranspiration*, T. A. Black, D. L. Spittlehouse, M. D. Novak, and D. T. Price, Eds., International Association of Hydrological Sciences, 13–20.
- Voogt, J. A., 2000: Image representations of urban surface temperatures. *Geo. Int.*, in press.
- , and T. R. Oke, 1997: Complete urban surface temperatures. *J. Appl. Meteor.*, **36**, 1117–1132.
- , and —, 1998a: Effects of urban surface geometry on remotely sensed surface temperature. *Int. J. Remote Sens.*, **19**, 895–920.
- , and —, 1998b: Radiometric temperatures of urban canyon walls obtained from vehicle traverses. *Theor. Appl. Climatol.*, **60**, 199–217.
- Wan, Z., and J. Dozier, 1989: Land-surface temperature measurement from space: Physical principles and inverse modeling. *IEEE Trans. Geosci. Remote Sens.*, **27**, 268–277.
- Webb, E. K., G. I. Pearman, and R. Leuning, 1980: Correction of flux measurements for density effects due to heat and water vapour transfer. *Quart. J. Roy. Meteor. Soc.*, **106**, 85–100.